INTERNATIONAL JOURNAL FOR NUMERICAL METHODS IN ENGINEERING
Int. J. Numer. Meth. Engng 2002; **54**:365–398 (DOI: 10.1002/nme.427)

Modelling of failure mode transition in ballistic penetration with a continuum model describing microcracking and flow of pulverized media

Benjamin A. Gailly[1] and Horacio D. Espinosa[2,*,†]

[1] *Délégation Générale pour l'Armement/Etablissement Technique de Bourges, Route de Guerry, 18015 Bourges Cédex, France*
[2] *Department of Mechanical Engineering, Northwestern University, 2145 Sheridan Road, Evanston, IL 60208-3111, U.S.A.*

SUMMARY

A new continuum model to describe damage, fragmentation and large deformation of pulverized brittle materials is presented. The multiple-plane-microcracking (MPM) model, developed by Espinosa, has been modified to track microcracking on 13 orientations under high pressure, high strain rate and high deformation. This model provides the elastic and inelastic response of the material before massive crack coalescence. When pulverization occurs, the constitutive response is modelled by means of a visco-plastic model for granular material, which is a generalization to three dimensions of the double-sliding theory augmented by a consolidation mechanism. The initialization of the granular model is governed by a yield surface at the onset of massive crack coalescence. This is accomplished by examining a representative volume element, modelled using the MPM model, in compression-shear. The main advantage of this approach is to keep a continuum model at all stages of the deformation process and thus avoid the difficulties of crack representation in a discrete finite element code. This model has been implemented in LS-DYNA and used to examine interface defeat of long rod penetrators by a confined ceramic plate. The numerical simulations are compared to experiments in order to identify failure modes. The model parameters were obtained *independently* by simulating plate and rod impact experiments. The proposed model captures most of the physical observations as well as failure mode transition, from interface defeat to full penetration, with increasing impact velocity. Copyright © 2002 John Wiley & Sons, Ltd.

KEY WORDS: granular materials; brittle materials; constitutive modelling; impact; ballistic penetration; damage; visco-plasticity

*Correspondence to: Horacio D. Espinosa, Department of Mechanical Engineering, Northwestern University, 2145 Sheridan Road, Evanston, IL 60208-3111, U.S.A.
†E-mail: espinosa@nwu.edu

Contract/grant sponsor: Army Research Office; contract/grant number: DAAH04-96-1-0331
Contract/grant sponsor: Delegation Generale pour L'Armement; contract/grant number: 21132/DGA/DSP/D

Published online 27 February 2002 — *Received 9 July 2000*
Revised 10 May 2001

1. INTRODUCTION

Ceramics present a high potential as armour materials. Their high compressive strength and low thermal conductivity could be used to defeat, not only low speed rigid body projectiles, but also high speed, heavy alloy, long rods. Unfortunately, hardness is often associated with brittleness and ceramics can undergo fragmentation when subjected to multiaxial loading. It is now well known that, during a high velocity impact event, a comminuted zone also called *Mescall zone*, Mescall and Weiss [1], appears under the projectile nose. The penetration of the projectile is controlled by the behaviour of the granular material and the intact surrounding ceramic, Shockey *et al.* [2]. Based on this understanding, a new armour concept has been proposed and improved by Hauver *et al.* [3, 4], Bless *et al.* [5], Rapacki *et al.* [6], Espinosa *et al.* [7] and Malaise *et al.* [8] in order to block the motion of the ceramic fragments.

During the same period, Orphal *et al.* [9–11] studied the response of confined AlN, SiC and B_4C ceramics during long rod penetration at velocities ranging from 1.5 to 5 km/s. They measured substantial data with the help of flash X-ray, e.g. penetration depth, rate of rod consumption, mass efficiency of the ceramic target, etc. All this information is extremely valuable in the development of advanced computational algorithms.

The interface defeat (ID) design was later improved by Bruchey *et al.* [12]. In this configuration, the ceramic tile is encapsulated in a titanium alloy structure that increases the mass efficiency of the target. In this particular configuration, the graphite plate is not needed to initiate the ID of the projectile.

More recently, Lundberg *et al.* [13] estimated the upper and lower bounds for the transition impact velocity between ID and normal penetration for steel and tungsten alloy projectiles and for two types of SiC, B_4C, TiB_2 and a polycrystalline diamond composite target materials. They also provided valuable X-ray pictures of the projectile inside the ceramic during the penetration process from which they extrapolated the projectile nose velocity.

In most of the ballistic experiments performed in the past the target configuration has a big influence on the establishment of ID phenomena. Malaise *et al.* [8] proposed an alternate configuration of impact resulting in the same physical phenomenon. The target configuration is the depth of penetration (DOP) configuration, but ID can be achieved by encapsulating the projectile in a polycarbonate cylinder. This configuration can be advantageously used to separate the influence of different parameters such as projectile velocity, mechanical characteristics of the ceramic and damage kinetics resulting from the separation between normal and shear waves. Furthermore, this configuration is easier to model when Lagrangian codes, using remeshing, are employed.

Although numerical analyses of high velocity impact and penetration have been carried out for quite some time, few applications to the response of ceramic targets have been made. The key issue is the appropriate modelling of the complex constitutive behaviour of ceramics in the presence of micro and macrocracks. Attempts have been made to model the inelastic constitutive behaviour of ceramics in the presence of cracks, and to validate the models through simulation of plate and rod impact experiments. Addesio and Johnson [14] presented a microphysical model to describe the confined behaviour of ceramics. The inelastic strains in their model are caused by microcracking. Cracks are allowed to slide under compression and open under tension. Damage is determined in terms of a crack density parameter whose evolution is described through a failure surface based on energy balance.

Rajendran and Grove [15] proposed a model considering microcrack nucleation and growth, and pore collapse. Damage is defined in terms of an average crack density, which is treated as an internal variable. The reduction in stiffness due to microcracking is modelled using damage moduli whose evolution under compressive as well as tensile loading is formulated based on the generalized Griffith criterion. Pore collapse is modelled using viscoplastic equations derived from Gurson's pressure dependant yield function, Gurson [16]. The Hugoniot elastic limit (HEL) scaled by a rate-dependant formulation gives the yield surface. Due to the isotropic formulation, this model is not capable of capturing anisotropic damage that develops especially under oblique impact. The material collapse occurs at deviatoric stresses above the HEL and does not take into account the porosity created by shearing of the pulverized ceramic. Moreover, the friction between fragments is not considered. Nevertheless, this model reproduces, with a good accuracy, the tension fracture occurring in normal plate impact experiments.

Based on dislocation theory, Curran *et al.* [17] proposed a computational model to describe penetration of ceramic targets through a multiple-plane phenomenological model. In their model, the deviatoric stress in the comminuted material is used to describe inelasticity and flow. Pressure is calculated by means of the standard Mie–Gruneisen equation of state for the intact material. A continuum porous compaction model accounting for the applied shear strain is used in the comminuted zone. Their yield function accounts for damage as well as Coulomb's friction. A tensile fracture model is used to allow the separation of fragmented particles. Curran and co-workers identified their model parameters from pressure–shear impact experiments and performed simulations of the confined ceramic targets tested by Shockey *et al.* [2]. Based on the simulations, they concluded that confining pressure and intergranular friction in the comminuted material are the key factors governing the penetration resistance of confined ceramics but they did not manage to simulate all the experimentally observed features. One of the major disadvantages in the use of this model is that the phenomenological parameters introduced to describe the various inelastic processes are difficult to identify experimentally. Moreover, they used nine planes to describe the deformation of the comminuted ceramic but it appears that the slip planes chosen are not isotropic by rotation and do not necessarily correspond to the maximum shearing plane in the material.

Johnson and Holmquist [18] proposed a more general model to represent the behaviour of brittle materials and transition between the intact and granular media. It assumes an elasto-plastic behaviour with a yield stress that depends on pressure and damage. The yield stress is interpolated between the yield stress of the intact ceramic and the yield stress of the fragmented ceramic. Both yield stresses are linear functions of the applied pressure while the damage parameter is related to the accumulated plastic strain normalized by the strain at rupture, which is also a function of pressure. Despite the pressure dependence of the model, Malaise *et al.* [8] has shown that this model cannot capture the transition between penetration and ID. The reason advanced is that compaction of the granular ceramic is not properly accounted for and that damage under tension is overestimated.

Enhancing the model of Johnson and Holmquist [18], Collombet *et al.* [19] developed an engineering model, which was implemented in a Eulerian code. Their model describes fragmentation and separation of fragments by two distinct damage variables. One such variable is the function of plastic shear strain to account for microcrack nucleation resulting from plastic deformation. When this damage parameter reaches a percolation value, the media is considered fully fractured. The tensile damage variable is related to the sum of the principal tensile strains and assumes that initial porosity is very small; hence, compaction is not possible. The yield stress of the damaged ceramic has a linear dependency on pressure until it reaches the HEL where the ceramic becomes fully plastic. The yield function of the fragmented ceramic is a Mohr–Coulomb type yield surface. Despite the fact that dilatancy is not taken into account, this model has been used to reproduce ID in the configuration proposed by Malaise *et al.* [8]. Nevertheless, Malaise considered that friction between fragments in the comminuted zone is very small ($\mu = 10^{-3}$) which contradicts the measurement of μ in pressure–shear plate impact experiments performed by Klopp and Shockey [20] and Sairam and Clifton [21]. Moreover, the model is fully isotropic and therefore cannot capture damage anisotropy as observed in oblique impact.

To overcome the limitation of the phenomenological models previously mentioned and in particular, damage anisotropy as well as difficulties in determining model parameters, Espinosa [22] developed a multi-plane microcracking (MPM) model based on the theory of micromechanics of solids. In the MPM model, the constitutive response of the material is obtained from fundamental quantities that can be determined experimentally such as grain size and fracture toughness. In addition, since dynamic growth of microcracks is described independently on each orientation, damage anisotropy and rate effects are naturally incorporated in the model. This model does not include crack coalescence. Therefore, it cannot fully capture the constitutive behaviour of pulverized ceramics. However, it provides the deformation history leading to ceramic powders.

Camacho and Ortiz [23] and Ortiz [24] modelled ballistic penetration of ceramic targets based on a discrete fragmentation approach. In this approach, each crack is followed as it nucleates, propagates and coalesces during the deformation process. Cracks can nucleate at the nodes of a finite element mesh as soon as the resolved effective stress exceeds the effective fracture stress. The crack is nucleated in the solid by duplicating nodes and can propagate along element boundaries. Adaptive remeshing is used to reach enough sets of possible fracture paths around the crack tip. Following this procedure, fragments are generated as the cracks coalesce and bound a sub-body. The models and algorithms developed by Ortiz's group have been very successful in capturing penetration modes. They have shown that mushrooming and petaling of the tip of WHA penetrators, plus some sloughing of fragments, are the dominant deformation mechanisms controlling the penetration process.

Espinosa *et al.* [25] showed that pure discrete cohesive models may not be able to capture the right amount of energy dissipation unless the two size scales, involving fracture, are properly captured. These are short microcracks within fragments and coalesced microcracks forming the fragments, see Reference [25]. Consequently, a discrete cohesive model requires a mesh size consistent with the maximum possible *surface energy per unit volume* the material is capable of dissipating. Recently, powerful methods to capture arbitrary three dimensional dynamic propagation of cracks in elastic solids were developed by Belytschko *et al.* [26, 27]. Here, we examine an alternative approach to the discrete cohesive model in relation to the physical modelling of ballistic penetration of multi-layered targets.

Gu *et al.* [28] formulated a model for granular materials that we will make use of in this article. The model has a *two-mechanism* yield surface accounting for material flow under shearing and consolidation under pressure. The *distortion* mechanism is a Mohr–Coulomb type with a shear stress limitation at high pressure to take into account plastic deformation of the particles. Dilatancy and cohesion are included and depend on friction coefficient and on void ratio. The friction coefficient has an evolution law that can be easily determined and mainly depends on void ratio. A quarter elliptical pressure cap mathematically describes the consolidation mechanism. This mechanism accounts for void collapse. The pressure cap depends only on void ratio.

One of the difficulties in describing the comminuted zone in a ceramic by a granular model is that the characteristics of the powder, e.g., average size, often has to be assumed before carrying on the computation. Hence, the description of the powder state is somewhat arbitrary. Moreover, the void ratio in the fragmented ceramic is very low and determination of an initial friction coefficient in the comminuted ceramic cannot be easily performed. Here, we describe a computational scheme that bridges the MPM and granular models and overcomes these difficulties. Standard homogenization techniques and the MPM are used for this purpose. Damage initiation and material pulverization are captured in a single continuum theory.

The organization of the paper is as follows. In Section 2, we describe the MPM model, the extension of the granular model proposed by Anand and its use in conjunction with the MPM model. The main idea is to follow the fracture process by the MPM model until fragments due to crack coalescence are formed. The motion of the fragments is then computed with the modified granular model. The key point is that the characteristic of the powder is not assumed but computed from the ceramic response. The initial parameters of the granular model are determined by interrogating a representative volume element described by the MPM model. The only required parameters in the granular model are those describing the evolution of the internal quantities. These parameters were determined independently by models performed on ceramic powders with a known void ratio, Espinosa and Gailly [29]. In Section 3, we use this model to simulate the encapsulated rod experiments proposed by Malaise *et al.* [8]. The simulations are complemented by a parametric study on the effect of the various material properties on ballistic penetration.

2. CONSTITUTIVE EQUATIONS

2.1. Multi-plane microcracking model

The large deformation constitutive response of ceramics in the presence of microcracks is described through a microcracking multiple-plane model based on a dilute approximation, Dienes [30], Bazant and co-workers [31], Espinosa [32] and Espinosa *et al.* [22, 25, 33]. The basic assumption is that microcracking and/or slip can occur on a discrete number of orientations (see Figure 1). Microcrack plane properties (friction, initial size, density, etc.) and their evolution are *independently* computed on each plane. The macroscopic response of the material is computed by additive decomposition of the strain rate tensor, D, into elastic, D^{e}, and inelastic parts, D^{c}. The inelastic strains are assumed to be caused solely by the presence of microcracks in the solid.

Using a corrotational Cauchy stress measure, T^{∇}, the constitutive behaviour of the ceramic is given by

$$T^{\nabla} = C\lfloor D - D^{\mathrm{c}} \rfloor \tag{1a}$$

where C is the fourth order elasticity tensor of the polycrystalline ceramic material.

For a representative volume B_0, in the undeformed configuration, of an elastic solid containing penny-shaped microcracks with a density $N^{(k)}$, the average inelastic strain rate tensor

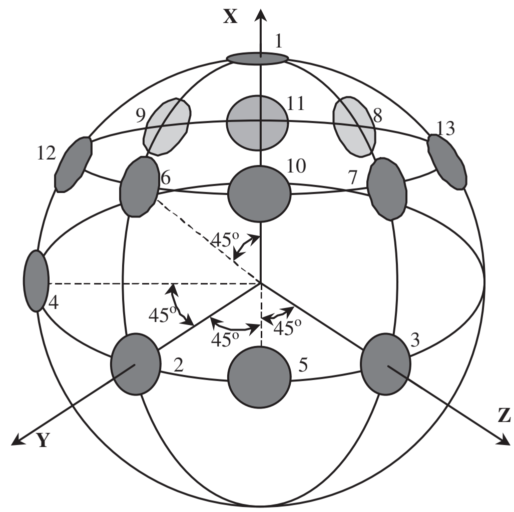

Figure 1. Unit sphere containing 13 microcracking orientations. Each orientation has a density $N^{(k)}$.

can be written as

$$\dot{D}^{c}_{ij} = \sum_{k=1}^{13} N^{(k)}\pi \left(a^{(k)}\right)^2 \frac{1}{2}\left(\dot{\bar{b}}^{(k)}_i n^{(k)}_j + n^{(k)}_i \dot{\bar{b}}^{(k)}_j\right) + \sum_{k=1}^{13} N^{(k)}\pi a^{(k)}\dot{a}^{(k)}\frac{1}{2}\left(\bar{b}^{(k)}_i n^{(k)}_j + n^{(k)}_i \bar{b}^{(k)}_j\right) \tag{1b}$$

where the subindex k is used to label the orientations. In the above equation, $a^{(k)}$ and $\dot{a}^{(k)}$ denote, respectively, the microcrack radius and its rate of growth on orientation k, $n^{(k)}$ is the corresponding unit normal, and $\bar{b}^{(k)}$ and $\dot{\bar{b}}^{(k)}$ are the average displacement jump vectors across the surface $A^{(k)}$ and its rate.

The average displacement jump vector resulting from an applied Cauchy stress field T is given by Equation (2a) in tension and Equation (2b) in compression, viz.

$$\bar{b}^{(k)}_i = \frac{1}{A^{(k)}}\int_{A^{(k)}} b^{(k)}_i \,\mathrm{d}A = \frac{16(1-v^2)}{3\pi E(2-v)} a^{(k)}\left(2T_{ij}n^{(k)}_j\right) - vT_{jl}n^{(k)}_j n^{(k)}_l n^{(k)}_i \tag{2a}$$

$$\bar{b}^{(k)}_i = \frac{32(1-v^2)}{3\pi E(2-v)} a^k \left(\tau^k + \mu^{(k)}\sigma^k_n\right)(n_\tau)^k_i \tag{2b}$$

in which E and v are Young's modulus and Poisson's ratio of the uncracked solid, τ^k and σ^k_n are the resolved shear stress and the normal stress acting on microcracks with orientation k, and n^k_τ is the unit vector in the direction of the resolved shear traction. In Equation (2b), $\mu^{(\kappa)}$ is the friction coefficient on the microcrack faces. Its dependence on the normal stress, applied on the crack faces, is given by

$$\mu^{(k)} = \mu_{\min} + (\mu_{\max} - \mu_{\min})\frac{2}{\pi}\arctan\left(\frac{-\sigma_n^{(k)}}{p_\mu}\right) \quad \text{if } \sigma_n^{(k)} \leqslant 0$$
$$\mu^{(k)} = \mu_{\min} \quad \text{if } \sigma_n^{(k)} > 0 \tag{3}$$

where $\mu_{\min}$ and $\mu_{\max}$ are, respectively, the friction coefficients for a null normal stress and a high normal compression stress and p_μ is the normal stress for which $\mu^{(\kappa)} = 0.78\mu_{\max}$.

If $\tau^{(k)} \leqslant -\mu^{(k)}\sigma_n^{(k)}$, then a sticking condition occurs. Hence, irreversible displacement jumps develop making the deformation process strongly non-linear and history dependant. It should also be pointed out that, because of the dependence of the friction coefficient on the normal stress, the sticking condition can prevent the propagation of microcracks under high compression stress states.

In order to compute the inelastic strain tensor, it becomes necessary to follow the evolution of the microcrack radius a in the selected orientations. Following Freund [34], an equation of evolution for a in the case of mixed mode loading can be derived as,

$$\dot{a}^{(k)} = m^{\pm} c_{\mathrm{R}} \left[1 - \left(\frac{K_{\mathrm{Ic}}}{K_{\mathrm{eff}}^{(k)}}\right)^{n^{\pm}}\right] \geqslant 0 \tag{4}$$

in which $n^{\pm}$ and $m^{\pm}$ are phenomenological material constants which may have different values in tension and compression. They are used to describe terminal crack speeds of about 30 per cent the Rayleigh wave speed, C_{R}. K_{Ic} is the material toughness and K_{eff} is the effective stress intensity factor. For mixed mode conditions, K_{eff} for the particular orientation k is derived by considering the average energy release rate G associated with the increase in the radius of the microcrack whose radius is a. It is given by

$$G^{(k)} = \frac{1}{2\pi}\int_0^{2\pi} \frac{1-\nu^2}{E}[K_{\mathrm{I}}^2 + K_{\mathrm{II}}^2 + K_{\mathrm{III}}^2(1-\nu)] \tag{5}$$

from which the following expression for K_{eff} is obtained:

$$K_{\mathrm{eff}}^{(k)} = \sqrt{\frac{G^{(k)}E}{1-\nu^2}} \tag{6}$$

The general structure of these constitutive equations corresponds to that of a solid with a damage-induced anisotropic stress–strain relation with elastic degradation. The rate dependence is due to crack kinetics effects. From a computational standpoint, this ensures numerical reliability and mesh independence, Needleman [35]. Details about the stress update algorithm can be found in Espinosa [22]. It should be pointed out that this inelastic model is a *continuum* model in which material damage results from microcracking. If the material is subjected to a predominantly tensile stress state, then microcracks along orientations perpendicular to the direction of maximum tensile stresses will grow according to Equation (3). In this case, significant dilation is expected due to mode I crack opening. If a predominantly compressive state of stress with shear is imposed, then crack opening is inhibited but inelasticity is manifested by the growth of penny-shaped cracks in modes II and III (shear modes).

2.2. *Granular model*

Here, we describe a *two-mechanism* constitutive model previously developed by Anand and co-workers [2] to describe the isothermal deformation of granulated media. The model is extended to the visco-plastic regime using the Duvaut Lions scheme, see Simo *et al.* [36].

Using a corrotational Cauchy stress measure, the constitutive behaviour of the powder is given by

$$T^{\nabla} = C(\mathbf{T}, \eta)[D - D^{\mathrm{p}}] \tag{7a}$$

where C is the fourth order elasticity tensor that depends on the relative density $\eta = \rho/\rho_{\mathrm{s}}$. Here, ρ is the mass density of the granular material and ρ_{s} is the mass density of solid particles. D and D^{p} are, respectively, the deformation rate tensor and the plastic deformation rate tensor, which is the sum of the contribution of the two mechanisms. In this model it is assumed that the plastic spin, $\mathbf{W}^{\mathrm{P}}$, is zero. For a justification on this assumption, see Anand and Gu [28]. The symmetric Cauchy stress tensor can be written in terms of its spectral components, namely,

$$\mathbf{T} = \begin{cases} \sigma_1\, \widehat{\mathbf{e}}_1 \otimes \widehat{\mathbf{e}}_1 + \sigma_2\, \widehat{\mathbf{e}}_2 \otimes \widehat{\mathbf{e}}_2 + \sigma_3\, \widehat{\mathbf{e}}_3 \otimes \widehat{\mathbf{e}}_3 & \text{if } \sigma_1 > \sigma_2 > \sigma_3 \\ \sigma_1\, \widehat{\mathbf{e}}_1 \otimes \widehat{\mathbf{e}}_1 + \sigma_3 (1 - \widehat{\mathbf{e}}_1 \otimes \widehat{\mathbf{e}}_1) & \text{if } \sigma_1 > \sigma_2 = \sigma_3 \\ \sigma_3\, \widehat{\mathbf{e}}_3 \otimes \widehat{\mathbf{e}}_3 + \sigma_1 (1 - \widehat{\mathbf{e}}_3 \otimes \widehat{\mathbf{e}}_3) & \text{if } \sigma_1 = \sigma_2 > \sigma_3 \end{cases} \tag{7b}$$

where $\{\sigma_i \mid i = 1, 2, 3\}$ are the principal stresses and $\{\widehat{\mathbf{e}}_1 \mid i = 1, 2, 3\}$ are the principal directions of stress. The usual solid mechanics convention of sign is employed, i.e. positive values correspond to tensile stresses.

The elastic properties of the granular material, i.e. Young's modulus, E, and Poisson's ratio, v, are predetermined by means of the self-consistency method proposed by Budianski [37], and then fitted to the functions,

$$E = E_1 \mathrm{e}^{E_2 \eta} \tag{8}$$

$$v = v_1 \mathrm{e}^{-v_2 \eta} \tag{9}$$

These quantities fully define $C(\mathbf{T}, \eta)$ given in Equation (7a).

The first mechanism called *distortion* employs a pressure-sensitive, Mohr–Coulomb type yield condition with a non-associated flow rule, i.e.

$$\phi^{(1)} = \{\tau - s(\sigma)\} \leqslant 0 \quad \text{with } s(\sigma) = c + s^* \left\{ \tanh\left(\frac{\mu\sigma}{s^*} \right) \right\} \tag{10}$$

where τ and σ represent, respectively, the resolved shear stress and the normal stress on a preferred slip plane, $s(\sigma)$ is a function that describes the sensitivity of the yield surface to the cohesion of the material, c, and s^* is the shear strength of the powder at high pressure. This shear strength is considered a constant.

A pair of orthonormal vectors $(\mathbf{m}^{(\alpha)}, \mathbf{n}^{(\alpha)})$ define each slip plane, as explained in Gu *et al.* [28]. The potential slip systems are chosen such that the yield function $\phi^{(1)}$ is a maximum.

This results in

$$\tau = \tfrac{1}{2}\sin(2\xi)(\sigma_1 - \sigma_3) \geqslant 0 \tag{11}$$

$$\sigma = -\tfrac{1}{2}(\sigma_1 + \sigma_3) + \tfrac{1}{2}\cos(2\xi)(\sigma_1 - \sigma_3) \tag{12}$$

with

$$\xi = \pm\left\{\frac{\pi}{4} + \frac{\phi}{2}\right\}$$

in which $\phi = \arctan(\tilde{\mu})$, and

$$\tilde{\mu} = \frac{\mathrm{d}s}{\mathrm{d}\sigma} = \left\{\frac{\mu}{\cosh^2}(\mu\sigma/s^*)\right\} \tag{13}$$

in the above equations, σ_1 and σ_3 are the first and third principal stresses.

The cohesive strength depends only on the relative density η and is given by the following functional relation:

$$c = \begin{cases} A\eta^m \dfrac{(\eta - \eta_m)}{(1 - \eta_m)} & \text{if } \eta > \eta_m \\ 0 & \text{if } \eta \leqslant \eta_m \end{cases} \tag{14}$$

A and m are material constants and η_m is a characteristic density.

The friction coefficient μ depends on η and the plastic deformation. Its evolution equation is given by

$$\dot{\mu} = h(\mu)\dot{\gamma}^{(1)} \quad \text{with the initial condition } \mu(0) = \mu_0 \tag{15}$$

$$h(\mu) = h_\mu \left|\left(1 - \frac{\mu}{\mu_{\mathrm{s}}}\right)\right|^p \operatorname{sign}\left(1 - \frac{\mu}{\mu_{\mathrm{s}}}\right) \tag{16}$$

$$\mu_{\mathrm{s}} = \begin{cases} \mu_{\mathrm{cv}} + b(\eta - \eta_{\mathrm{cr}})^q & \text{if } \eta > \eta_{\mathrm{cr}} \\ \mu_{\mathrm{cv}} & \text{if } \eta \leqslant \eta_{\mathrm{cr}} \end{cases} \tag{17}$$

where μ_{s} is the saturation value of μ.

Quantities p, q, b, η_{cr}, μ_{cv} and h_μ are material parameters. The plastic shear strain rate $\dot{\gamma}^{(1)}$ is determined by the flow rule

$$D^{\mathrm{p}(1)} = \dot{\gamma}^{(1)} M^{(1)} \tag{18}$$

$$\mathbf{M}^{(1)} = \frac{\mathbf{P} + \beta\mathbf{N}}{\|\mathbf{P} + \beta\mathbf{N}\|} \tag{19}$$

$$\beta = h_\beta(\mu - \mu_{\mathrm{cv}}) \tag{20}$$

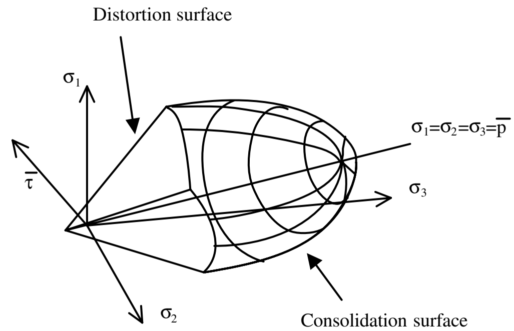

Figure 2. Yield surfaces for the granular model. There is a non-smooth intersection between the two surfaces.

in which h_β is another material parameter. The two tensors $\mathbf{P}$ and $\mathbf{N}$ are given in terms of $\mathbf{m}^{(\alpha)}$ and $\mathbf{n}^{(\alpha)}$, viz.

$$\mathbf{P} = \mathrm{sym}(\mathbf{m}^{(\alpha)} \otimes \mathbf{n}^{(\alpha)}); \quad \mathbf{N} = \mathbf{n}^{(\alpha)} \otimes \mathbf{n}^{(\alpha)} \tag{21}$$

Since $\mathbf{m}^{(\alpha)}$ and $\mathbf{n}^{(\alpha)}$ are a function of the principal stresses, three cases need to be considered:

Case (i): $\sigma_1 > \sigma_2 > \sigma_3$

$$\mathbf{P} = (\tfrac{1}{2})\sin(2\xi)\{\widehat{\mathbf{e}}_1 \otimes \widehat{\mathbf{e}}_1 - \widehat{\mathbf{e}}_3 \otimes \widehat{\mathbf{e}}_3\} \tag{22}$$

$$\mathbf{N} = \{\sin^2\xi\, \widehat{\mathbf{e}}_1 \otimes \widehat{\mathbf{e}}_1 + \cos^2\xi\, \widehat{\mathbf{e}}_3 \otimes \widehat{\mathbf{e}}_3\} \tag{23}$$

Case (ii): $\sigma_1 > \sigma_2 = \sigma_3$

$$\mathbf{P} = (\tfrac{1}{2})\sin(2\xi)\{\widehat{\mathbf{e}}_1 \otimes \widehat{\mathbf{e}}_1 - (\tfrac{1}{2})(1 - \widehat{\mathbf{e}}_1 \otimes \widehat{\mathbf{e}}_1)\} \tag{24}$$

$$\mathbf{N} = \{(\tfrac{1}{2})\sin^2\xi\, \widehat{\mathbf{e}}_1 \otimes \widehat{\mathbf{e}}_1 + (\tfrac{1}{2})\cos^2\xi(1 - \widehat{\mathbf{e}}_1 \otimes \widehat{\mathbf{e}}_1)\} \tag{25}$$

Case (iii): $\sigma_1 = \sigma_2 > \sigma_3$

$$\mathbf{P} = (\tfrac{1}{2})\sin(2\xi)\{(\tfrac{1}{2})(1 - \widehat{\mathbf{e}}_3 \otimes \widehat{\mathbf{e}}_3) - \widehat{\mathbf{e}}_3 \otimes \widehat{\mathbf{e}}_3)\} \tag{26}$$

$$\mathbf{N} = (\tfrac{1}{2})\{(\tfrac{1}{2})\sin^2\xi(1 - \widehat{\mathbf{e}}_3 \otimes \widehat{\mathbf{e}}_3) + \cos^2\xi\, \widehat{\mathbf{e}}_3 \otimes \widehat{\mathbf{e}}_3\} \tag{27}$$

The second mechanism, called *consolidation* represents the hardening of the media when voids collapse. It has a quarter-elliptical yield surface in the plane $(\bar{p}, \bar{\tau})$, where $\bar{p}$ and $\bar{\tau}$ are, respectively, the mean pressure and the equivalent shear stress (see Figure 2). The yield condition in this case is

$$\phi^{(2)} = \sqrt{\left(\bar{p} - \frac{p_c}{2}\right)^2 + \left(\frac{\bar{\tau}}{\mathbf{M}}\right)^2} - \frac{p_c}{2} \leqslant 0 \quad \text{for } \bar{p} > \frac{p_c}{2} \tag{28}$$

in which p_c is a limiting pressure that depends on the relative density η and M which is a shape parameter that depends on the material. In this formulation, p_c is assumed as

$$p_c = \begin{cases} B\eta^n \dfrac{(\eta - \eta_m)}{1 - \eta} & \text{if } \eta > \eta_m \\ 0 & \text{if } \eta \leqslant \eta_m \end{cases} \tag{29}$$

This equation for the pressure cap has been modified from the original function reported in Gu *et al.* [28] to take into account that, in our application, the material evolves from a fully dense solid to a pulverized media. Note that $p_c \to \infty$ when $\eta \to 1$ taking into account that pore collapse cannot occur on a fully dense powder.

The flow rule for the consolidation mechanism is an associated flow rule, namely,

$$D^{p(2)} = \dot{\gamma}^{(2)}\mathbf{M}^{(2)}; \quad \mathbf{M}^{(2)} = \partial\phi^{(2)}/\partial\mathbf{T} \tag{30}$$

see Gu *et al.* [28] for additional details.

In addition, the relative density η is calculated from balance of mass, viz.

$$\dot{\eta} = -\eta\, \mathrm{trace}(D^{\mathrm{p}^{(1)}} + D^{\mathrm{p}^{(2)}}); \quad \eta(0) = \eta_0 \tag{31}$$

The granular model developed by Gu *et al.* [28] has been primarily defined for compressive stress states. Here it is extended to tensile stress states by considering that the mean tensile stress in the material is limited by a value $-p_0$ for which the shear stress is null. The expression for this tensile mean stress is

$$p_0 = -\frac{s^*}{\mu} \tanh^{-1}\left(\frac{c}{s^*}\right) \tag{32}$$

An extended Duvaut–Lions viscoplasticity model [36] is used to introduce rate dependence in the above plasticity model. In this case, the viscoplastic strain rate and internal variables are given by

$$D^{\mathrm{vp}} = C^{-1}\left\{\frac{\mathbf{T} - \bar{\mathbf{T}}}{T_{\mathrm{R}}}\right\}; \quad \mathbf{q} = -\left\{\frac{\mathbf{q} - \bar{\mathbf{q}}}{T_{\mathrm{R}}}\right\} \tag{33}$$

where

$$(\bar{\mathbf{T}}, \bar{\mathbf{q}}) = \left\{ \begin{array}{ll} (\mathbf{T}, \mathbf{q}) & \text{if } \phi^{(1-2)} < 0 \\ \hat{\mathbf{P}}(\mathbf{T}, \mathbf{q}) & \text{otherwise} \end{array} \right\}$$

In these equations, $\mathbf{q}$ designates the internal variables vector, $\hat{\mathbf{P}}$ is the *closest point projection operator* and T_{R} is a viscosity coefficient that plays the role of a relaxation time. The viscoplastic deformation rate tensor is proportional to the distance between the stress state $\mathbf{T}$ and its projection onto the yield surface. Integration of the above equation leads to the following discrete expressions for the viscoplastic stress and internal variables, viz.

$$\mathbf{T}_{n+1} = \exp(-\Delta t/T_{\mathrm{R}})\mathbf{T}_n + [1 - \exp(-\Delta t/T_{\mathrm{R}})](\bar{T}_{n+1} + \mathbf{T}_{\mathrm{trial}} T_{\mathrm{R}}/\Delta t) \tag{34}$$

$$\mathbf{q}_{n+1} = \exp(-\Delta t/T_{\mathrm{R}})\mathbf{q}_n + [1 - \exp(-\Delta t/T_{\mathrm{R}})]\bar{\mathbf{q}}_{n+1} \tag{35}$$

where Δt is the time increment, $\mathbf{T}_{\mathrm{trial}}$ is the trial stress obtained by assuming elastic response in the increment, and $\bar{\mathbf{T}}$ and $\bar{\mathbf{q}}$ are obtained from the solution of the rate-independent plasticity problem. Note that for $T_{\mathrm{R}} \to \infty$ the elastic case is obtained while for $T_{\mathrm{R}} \to 0$ the rate independent plasticity solution is recovered.

2.3. Transition between damaged material represented by the MPM model to pulverized material represented by the granular model

Several criteria have been examined to switch from one model to the other. The relative density by itself is not a good parameter because under compression and shearing cracks can grow without any significant normal opening so η remains closer to 1. The sum of the crack length over the 13 orientations seems to be a better choice. If the cracks propagate along the 13 orientations then small fragments will be formed. If, on the contrary, there is one or few orientations in which crack growth occurs, then one can assume that bigger fragments will be formed and the total length of the cracks will remain approximately constant. In this criterion, the crack opening is not taken into account. The cracking effective strain is also a good candidate because it describes damage due to propagation and opening of microcracks. However, very large cracks can result while the cracking effective strain may still be small. To avoid this problem it has been decided to associate this last criterion with a limiting length of any microcrack on any orientation.

To ensure consistency during the transition, the initial values of the internal variables associated with the two mechanisms of the granular model must be obtained from the last state computed with the MPM model. For the distortion mechanism, these values are the initial relative density η_0, the initial friction coefficient μ_0, the cohesion of the fragmented ceramic, c_0, and the shear stress at high pressure, $s^* + c$. For the consolidation mechanism they are the initial pressure cap p_{c} and the shape parameter $\mathbf{M}$.

Based on the values of crack radius $a^{(k)}$, the normal average displacements jump $\bar{b}_n^{(k)}$ and the density of microcracks $N^{(k)}$ along each orientation k, it is possible to compute the relative density η of the cracked material compared to the uncracked material. For penny-shaped microcracks η is given by

$$\eta = 1 - \sum_{k=1}^{13} N^{(k)} 2\pi a^{(k)^2} \bar{b}_n^{(k)} \tag{36}$$

Furthermore, for small and moderate pressures, the friction coefficient is the slope of the yield curve in the space $(\bar{\tau}, \bar{p})$. By quasi-statically examining a representative volume element, for different shear/pressure ratios, until the growth of a microcrack on any of the 13 orientations is detected, the yield surface and its slope are determined (see Figure 3). In this calculation, a representative volume element with internal variables obtained from the MPM model is utilized. The cohesion is deduced from Equation (10) for a null pressure. For high pressure, the MPM model and the granular model predict that the shear stress has a

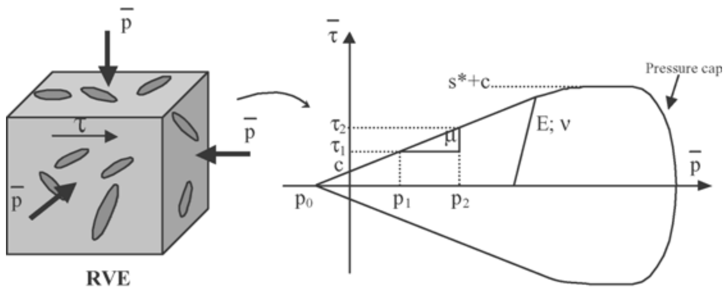

Figure 3. Interrogation of a representative volume element (RVE). States (τ_1, p_1) and (τ_2, p_2) are used to determine μ and c. The elastic properties E and v are computed for the maximum shear stress that does not lead to microcrack propagation.

limiting value, $s^* + c$. A high pressure is applied to the representative volume element and the shear/pressure ratio is increased until the yield surface is reached. By interrogating the representative volume element at high pressures, parameter s^* is determined.

The consolidation mechanism describes the collapsing of voids in the granular media. The shape parameter $\mathbf{M}$ is a constant while the pressure cap parameter p_c described a mechanism not taken into account in the MPM model. Hence, these two parameters are left as quantities to be identified by other means.

Finally, the Young's modulus and Poisson's ratio are initialized to the apparent Young's modulus and Poisson's ratio of the damaged ceramic by adjusting the values of E_1 and v_1. Thus, it is supposed that the shapes of Equations (8) and (9) remain the same when cracks propagate, while the initial apparent modules are degraded. The apparent elastic properties are determined during the search of the yield surface at low pressures. The bulk modulus is first calculated to average the anisotropy of the MPM model. Then, the shear modulus is obtained from the ratio σ_{12}/γ_{12}. In the current implementation only one shearing direction is tested because all calculations have been performed in an axial–symmetric configuration. There are no difficulties in extending this scheme to 3D, by also testing the shearing direction 13 and 23 and averaging the shear modulus over the three directions.

3. ANALYSES AND RESULTS

The constitutive equations described in the previous section have been implemented in the Lagragian/ALE code LS-DYNA. They have been used to carry out axisymmetric two-dimensional analysis of high velocity impact (1450–1900 m/s) and penetration of multi-layered ceramic target plates in DOP and ID configurations reported by Malaise *et al.* [28]. Then a parametric study has been conducted to determine the effect of material parameters on the results.

Despite the axial symmetry, the number of active planes is maintained equal to 13 but the density of crack in opposite planes has been set equal. Opposite planes are defined regarding symmetry with respect to the plane (O,x,y) when Oy is the axis of revolution. This way, crack extensions also remain equal in the opposite direction. Then, total shear stresses in the (O,x,z) and (O,y,z) planes are null. From a cell point of view, the axial symmetry condition is not violated and the influence of all planes is retained.

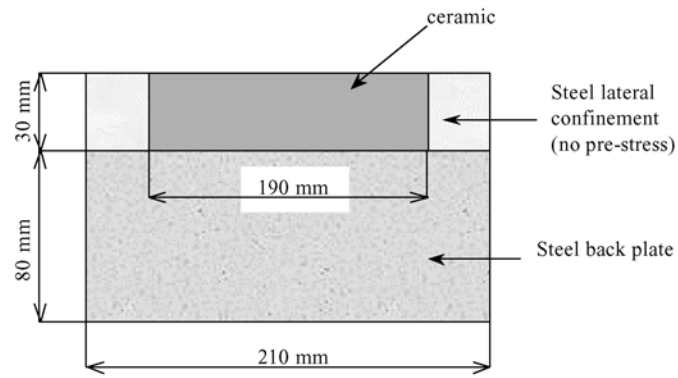

Figure 4. Multi-layered target used in DOP and ID configurations [3].

3.1. Configurations and material properties

The multi-layered target used in both, depth of penetration and ID configurations, is shown in Figure 4. The model previously discussed mathematically describes the ceramic elastic and inelastic behavior. The coefficients used in the simulations are summarized in Table I. No remeshing is allowed in the ceramic plate.

The steel used as a back plate is RHA steel while the lateral confinement is a mild steel ring. The properties of these materials are listed in Table II. In the simulations, an elastic constitutive behaviour is used for these two materials. The back steel plate thickness and lateral dimensions are the dimensions reported by Malaise *et al.* [28].

The projectiles simulated in the penetration configuration and in the ID configuration are shown, respectively, in Figures 5 and 6. In the penetration experiment, the projectile is not backed by a steel plate but by a titanium flyer. However, a steel back plate has been used in the simulations to limit the number of varying factors between the depth of penetration and the ID configurations. The steel back plate is simulated with an elastic constitutive law while the Johnson–Cook law [38] is used to model the tungsten heavy alloy (WHA) rod and the polycarbonate cylinder. The pressure in the rod and its confinement are computed with a Mie–Gruneisen type equation of state. The strain rate used in the Johnson–Cook laws is computed using a fully viscoplastic formulation. The plastic strain is obtained with a semi-implicit algorithm. The ALE feature of LS-DYNA models the WHA rod and its confinement. This avoids the problem of excessive element distortion.

3.2. Simulation results and comparison with experiments

Malaise's experiments have been carried out at a velocity of approximately 1450 m/s. X-ray pictures were obtained during the interaction between projectile and target. The efficiency of the configuration was characterized by the depth of penetration in the ceramic and eventually in the steel back-plate. Results and conditions of impact are summarized in Table III, Malaise *et al.* [28].

Utilization of the DOP configuration resulted in a complete penetration of the ceramic. On the contrary, the encapsulated WHA rod was completely defeated by the target at about the same impact velocity, see Table III. It has been verified that the impact of the polycarbonate

Table I. Material parameters for SiC used in the analyses.

Material's properties	Symbol	Units	SiC
Initial Young's modulus	E	GPa	420
Initial Poisson's ratio	v	—	0.1624
Initial density	ρ	kg/m^3	3177
Minimum internal friction coefficient	$\mu_{\mu iv}$	—	0.1
Maximum internal friction coefficient	$\mu_{\max}$	—	0.6
Normal stress shape	P_μ	GPa	15.0
Rayleigh wave speed	C_{R}	m/s	6871
Tenacity	K_{IC}	MPa$\sqrt{m}$	3.79
Initial crack radius	a_0	µm	1
Crack density in each orientation	$N^{(k)}$	/mm^3	1000
Crack velocity limitation factor in tension	m^+	—	0.3
Crack velocity limitation factor in compression	m^-	—	0.3
Crack velocity power in tension	n^+	—	0.3
Crack velocity power in compression	n^-	—	0.3
Maximum length of microcracks	$a_{\max}$	µm	500
Shape parameter for Young's modulus	E_2	—	5.0
Shape parameter for Poisson's ratio	v_2	—	0.412236
Consolidation mechanism	B	MPa	500.0
	n	—	2.84
	η_m	—	0.3
	M	—	1.2
Distortion mechanism	m	—	3.0
	h_μ	—	300.0
	p	—	1.88
	μ_{cv}	—	0.05
	b	—	0.071
	q	—	1.0
	η_{cr}	—	0.3
	h_β	—	2.0
Relaxation time	T_{R}	µs	10^{-13}
Limiting cracking strain	$\varepsilon_{\mathrm{cl}}$	—	0.15

cylinder alone causes no damage in the ceramic plate. All the computer simulations were performed with a velocity of 1450 m/s. The simulated penetration depths are summarized in Table IV. The end of computation refers to the time after impact of the rod on the front face of the ceramic. In the DOP configuration, usually the computation fails when elements in the ceramic plate are too distorted and the anti-hourglass algorithm becomes ineffective. In the ID configuration, however, the distortion remains low and the computations are stopped when the penetration velocity is null for several microseconds.

From the penetration depths shown in Table IV, it can be inferred that the model reproduces most of the phenomena experimentally observed. These results are the first of their kind in the sense that the physically based model, parametrically adjusted with other experimental configurations, can reproduce the observed failure mode transition.

In the depth of penetration configuration, the ceramic is pulverized by the impact and fragments are ejected as shown in Figure 7. The penetration history is shown in Figure 8. Although the computation stops after only a few microseconds, the process seems to reach a steady state. The penetration velocity is not strictly constant but oscillates between 600

Table II. Material properties of projectile and steel target plates used in analyses with LS-DYNA.

Material properties	Symbol	Units	WHA	RHA steel	Mild steel	Polycarbonate
Density	ρ	kg/m^3	17.30	7.85	7.85	1.19
Young's modulus	E	GPa	347	210	210	6
Poisson's ratio	v	—	0.3	0.3	0.3	0.28

Johnson–Cook model (1983)

$$\sigma = \lfloor C_1 + C_2\varepsilon^n \rfloor [1 + C_3 \ln \dot{\varepsilon}^*] \lfloor 1 - T^{*m} \rfloor$$
$$\dot{\varepsilon}^* = \dot{\varepsilon}/\dot{\varepsilon}_0; \quad \dot{\varepsilon}_0 = 1\ \mathrm{s}^{-1}$$
$$T^* = (T - T_{\mathrm{room}})/(T_{\mathrm{melt}} - T_{\mathrm{room}})$$

Material properties	Symbol	Units	WHA	RHA steel	Mild steel	Polycarbonate
Model constants	C_1	Mpa	926	—	—	420
	C_2	Mpa	843	—	—	343
	C_3	—	0.0385	—	—	0.01
	n	—	0.4	—	—	0.134
	m	—	0.5727	—	—	1.0
	T_{melt}	K	3000	—	—	388
	T_{room}	K	295	—	—	295

$$P = \frac{\rho_0 C^2 \mu [1 + (1 - \gamma_0/2)\mu - (a/2)\mu^2]}{[1 - (S_1 - 1)\mu - S_2\mu^2/(\mu + 1) - S_3\mu^3/(\mu + 1)^2]} + (\gamma_0 + a\mu)E_n \text{ for compressed materials}$$
$$P = \rho_0 C^2 \mu + (\gamma_0 + a\mu)E_n \text{ for expanded materials}$$
$$\mu = \rho/\rho_0 - 1$$

Material properties	Symbol	Units	WHA	RHA steel	Mild steel	Polycarbonate
EOS parameters	C	m/s	5196	—	—	1933
	S_1	—	−3.047	—	—	−3.49
	S_2	—	3.31	—	—	8.2
	S_3	—	−2.018	—	—	−9.6
	γ_0	—	1.58	—	—	0.61
	a	—	0	—	—	0
	E_{n0}	J/kg	0	—	—	0
Linear artificial viscosity	C_L	—	1.5	1.5	1.5	1.5
Quadratic artificial viscosity	C_Q	—	0.06	0.06	0.06	0.06
Specific heat	C_p	J/kg/K	134.5	—	—	125.6

Table III. Experimental configurations and penetration depth in SiC/steel plates [3].

Projectile configuration	V_{impact} (m/s)	Y_{aw} (°)	P_{SiC} (mm)	P_{steel} (mm)
Encapsulated WHA rod	1449	0.7	3	0
WHA rod	1462	2.7	30	4.5
PC cylinder/no rod	?	3.8	0	0

and 50 m/s as fragments are formed and ejected. During the first 5 μs, the pressure at the interface between the projectile and the ceramic is about 2 GPa (see Figure 9). This low pressure is the result of ejection of fragments and the low ceramic confinement. When a crater is formed and the ceramic is compacted on its edges, the pressure at the bottom of

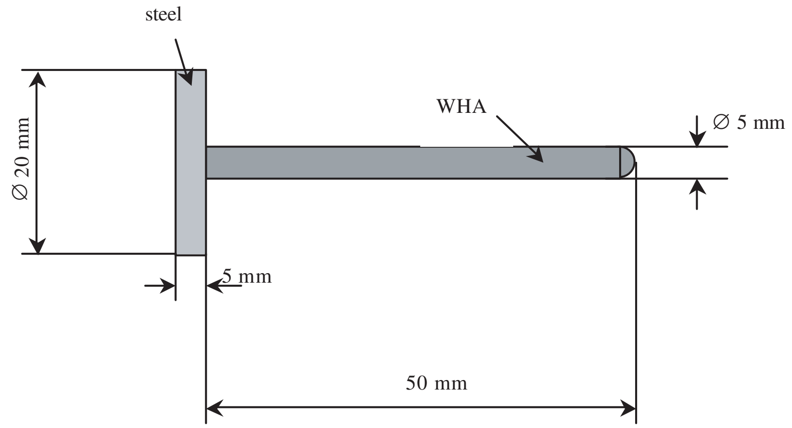

Figure 5. Projectile geometry used in the depth of penetration configuration.

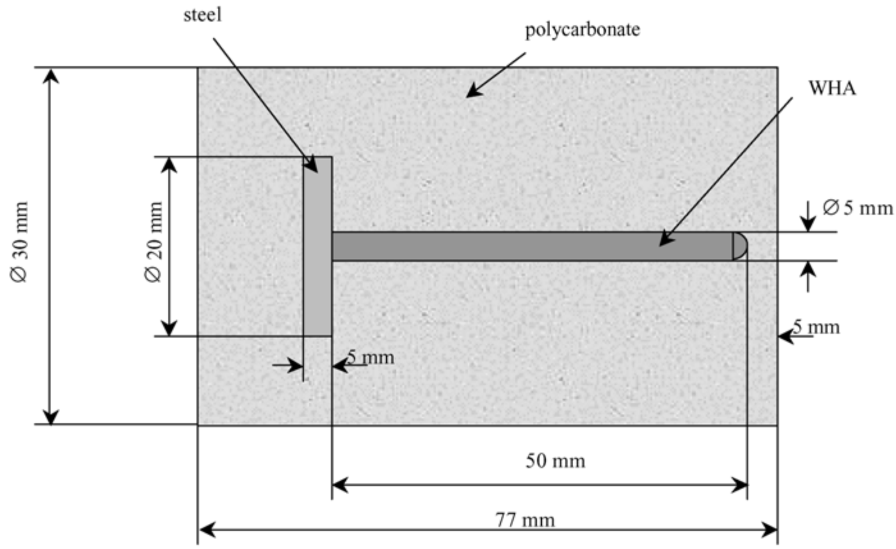

Figure 6. Projectile geometry used in the ID configuration.

Table IV. Simulated penetration depths for all configurations.

Projectile configuration	P_{SiC} (mm)	Penetration velocity (m/s)	End of computation (μs)
Encapsulated WHA rod	2.8	0	18.5
WHA rod	7.6	550	12.0
PC cylinder/no rod	0	0	45.0

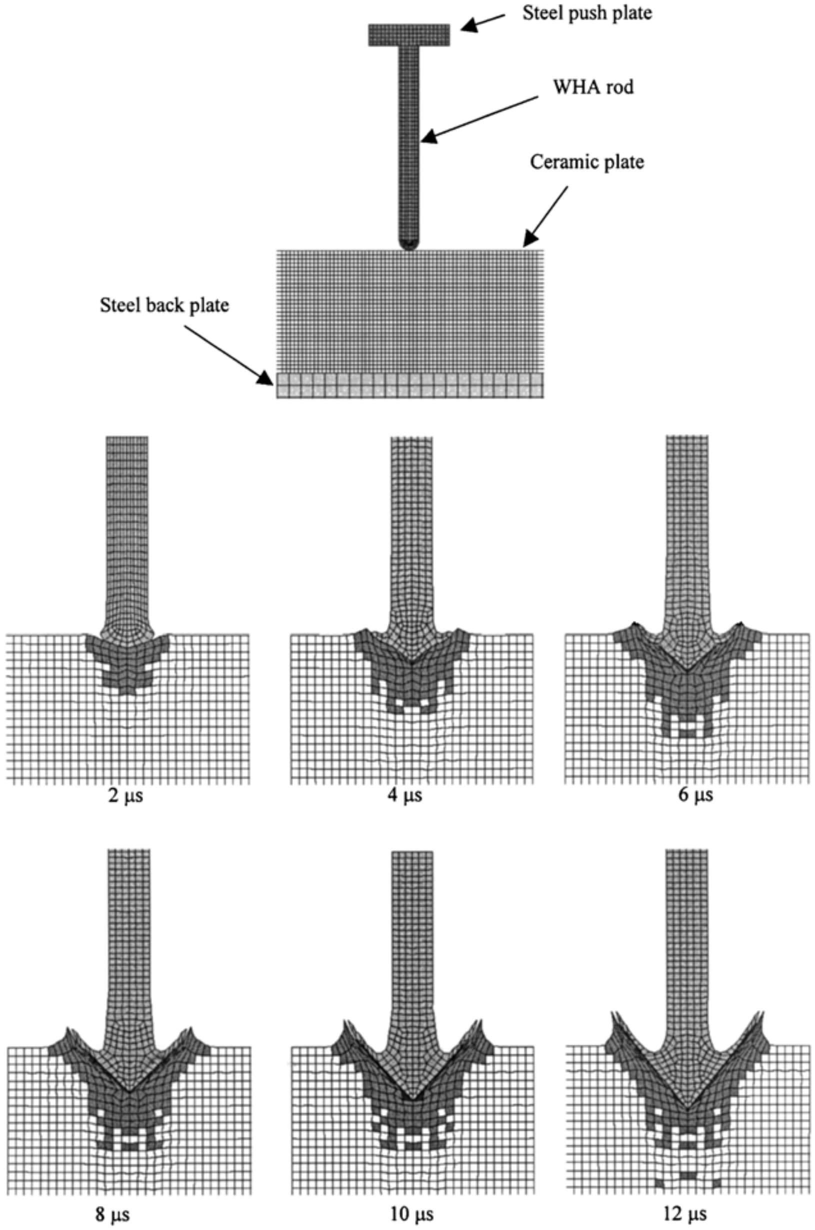

Figure 7. Simulation of depth of penetration configuration. Impact velocity 1400 m/s. Ejection of fragments is captured by the MPM-GRANULAR model. Shaded elements, at the penetrator–ceramic interface, are integrated using the granular model.

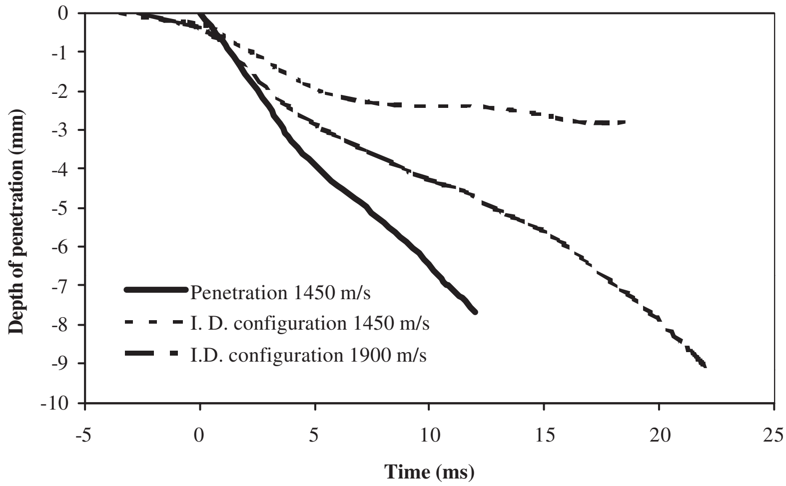

Figure 8. Depth of penetration versus time in the penetration and ID configurations. For $V_{\text{impact}} = 1900$ m/s, the projectile penetrates in the ID configuration. Time = 0 refers to the time at which the rod impacts the target.

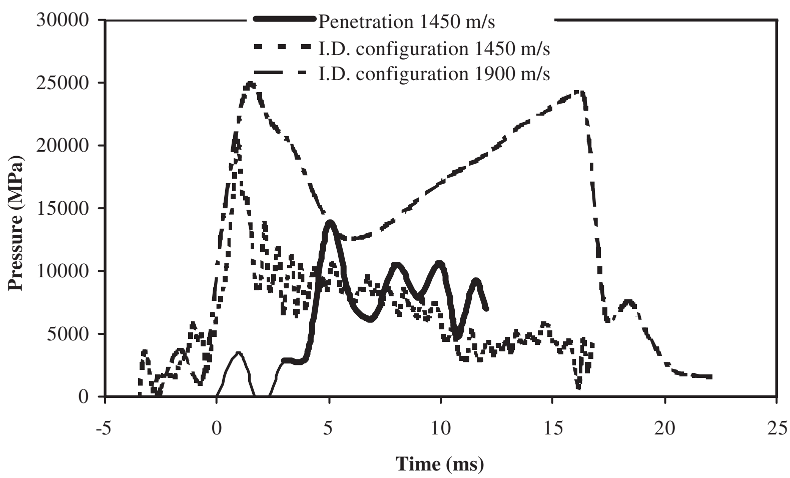

Figure 9. Pressure at the ceramic/projectile interface versus time. Time = 0 refers to the time at which the rod impacts the target.

the crater increases to 8 GPa, see Figure 9. The projectile mushrooms and is ejected with a velocity approximately equals to $-V_{\text{impact}}/2$. The penetration velocity decreases to 600 m/s. Extrapolating the penetration depth to the entire projectile consumption gives a penetration depth between 24 and 27 mm. This is similar to the experimental result if we consider that the penetration, in the steel plate, should have been made by the ceramic fragments and not by the projectile itself.

On the contrary, in the ID configuration, the pressure applied at the projectile/ceramic interface is equal to 5 GPa when the rod impacts. The fragments cannot be ejected and there is a pressure rise up to 20 GPa, see Figure 9. As the projectile flows on the front face of the ceramic, the pressure gradually decreases to 5 GPa. The projectile kinetic energy is not redirected forward but is applied on a larger area of the ceramic. This prevents the unstable propagation of cracks and results in less fragments being formed (see Figures 10–14). These fragments cannot be ejected because of the front confinement, so they contribute to the resistance to penetration. The projectile is soon defeated and the penetration velocity falls to zero.

It is worth noticing that the damage in the ceramic does not evolve when the ID phenomenon is established. The main implication is that the ratio L/D of the projectile should not have any influence on the efficiency of the target.

A beginning of spall plane can be seen and should be compared with the crack pattern on the recovered sample [28]. The total spall plane is not reproduced because a microcrack cannot propagate from one cell to its neighbours. Moreover, this is a typically discrete process that cannot be reproduced by the proposed model. Nevertheless, one cannot be sure that the spalling process occurs during the first stages of the impact or during the later ones, when the rarefaction waves arrive.

Just under the impact point, the ceramic seems to remain undamaged in this configuration. In the simulation, the relative density is everywhere higher than 0.95, which means that very few voids are created. Especially under the point of impact the relative density remains equal to 1, see Figure 10.

At 45° from the impact point, a cone-shaped zone of cracks is observed on the recovered samples. This pattern also appears in the simulation by plotting the length of the microcracks that develop at 45° with respect to the impact direction, see Figure 11.

An additional simulation has been carried out with an impact velocity of 1900 m/s (see Figures 8, 9 and 15). It is well known that ID is achieved only in a given range of impact velocity. It was not possible to investigate the low impact velocity region because the projectile behaviour changes drastically when the impact energy drops below a given value. In this case, projectile fracture is the preeminent phenomena. Nevertheless, at 1900 m/s, the simulation predicts a steady penetration rate. In the early stages, the pressure rises up to 25 GPa. A beginning of ID is achieved and the pressure drops to 13 GPa. Later on, deformation localizes under the impact point and pressure rises again to 25 GPa. The stress applied on the ceramic is sufficiently high to increase significantly the extent of the pulverized zone. The self-confinement of the ceramic is lost and penetration rate becomes steady. Finally, the pressure drops again before stabilizing to the same level as in the depth of penetration configuration.

The model with the chosen set of parameters is also able to capture the beginning of spalling during the impact of the polycarbonate cylinder. The crack cone on the rear face of the ceramic (see Figure 12) is also observed in the simulations. As in the experiment, the front face of the ceramic remains quasi-undamaged.

We have assumed in the MPM model that the ceramic remains elastic during the fracturing process. Similarly, when granulated, the ceramic remains elastic as long as the pressure is

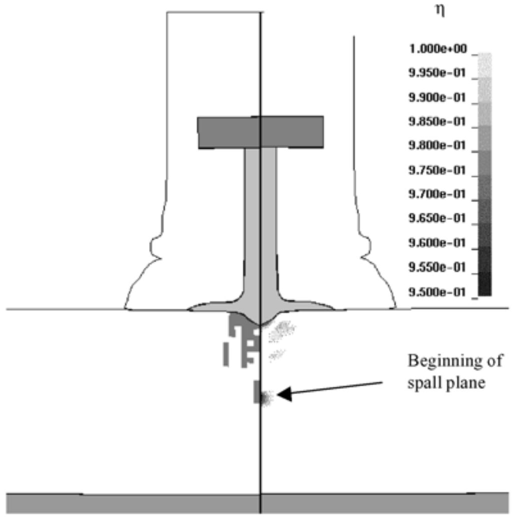

Figure 10. Relative density representing the apparent ceramic damage (right), elements being integrated using the granular model are shown in dark grey (left). ID configuration at 18.5 μs after rod impact.

below the cap value. When the powder is fully compacted, p_c asymptotically approaches infinity and the volumetric behaviour is fully elastic.

Collombet *et al.* [19] have determined a HEL of $-13.5\,$GPa for SiC. This is equivalent to a deviatoric stress of about 11 GPa. It has been verified that in the Mescal region the deviatoric stress in the ceramic remains most of the time below 11 GPa. Only very local zones reach states above this value and for short periods of time. Hence, the assumption of microcracking as the dominant inelastic mechanism during the deformation process is *a posteriori* verified within the framework of our model. Nonetheless, grain plasticity and twinning may occur in some small regions below the WHA projectile nose. These mechanisms are not directly accounted for in the MPM model.

Figures 13 and 14 show the penetration history, in the case of the ID configuration, at two impact velocities, 1450 and 1900 m/s, respectively. In the former case, the projectile transitions from a rod to a dish as a result of its continuous thermo-visco-plastic deformation at the ceramic surface. In the latter case, i.e. when the WHA rod impact velocity reaches 1900 m/s, the projectile is initially defeated, as evident from the mushrooming of the WHA penetrator. However, at about 14 μs, the projectile energy is again focused at the projectile nose and a more triangular deformation typical of steady-state penetration develops, see Figure 14. Unfortunately, this sharpening of the WHA penetrator cannot be verified experimentally by X-ray flash photography because of the dimensions and density of the confining material. It should be noted that no tip sharpening was observed in the ballistic penetration simulations performed by Camacho and Ortiz [39]. Their calculations exhibited mushrooming and petaling of the WHA penetrator tip plus some sloughing of fragments.

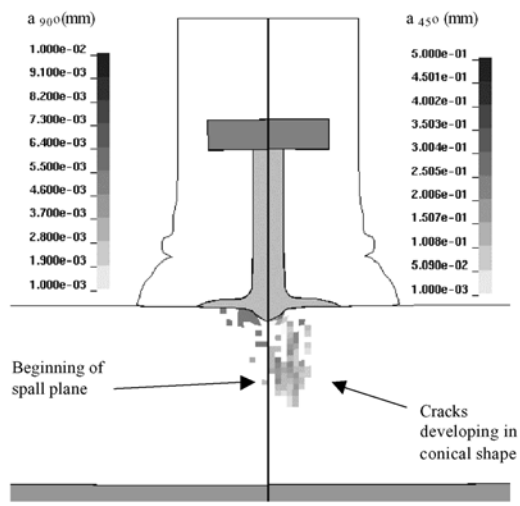

Figure 11. Contours of microcrack length at 90° (left) and 45° (right) from the direction of the projectile axis at 18.5 μs after rod impact.

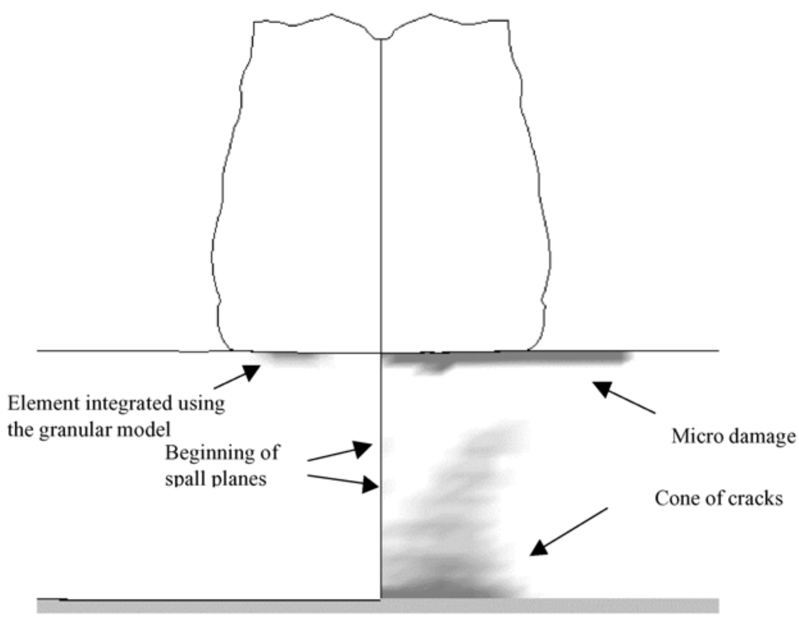

Figure 12. Polycarbonate cylinder configuration at 45 μs after impact. Inelastic effective strain (right) shows microdamage at the projectile–ceramic interface. Beginning of two spall planes and microcrack cone is observed. Element integrated using the granular model is shown in grey (left).

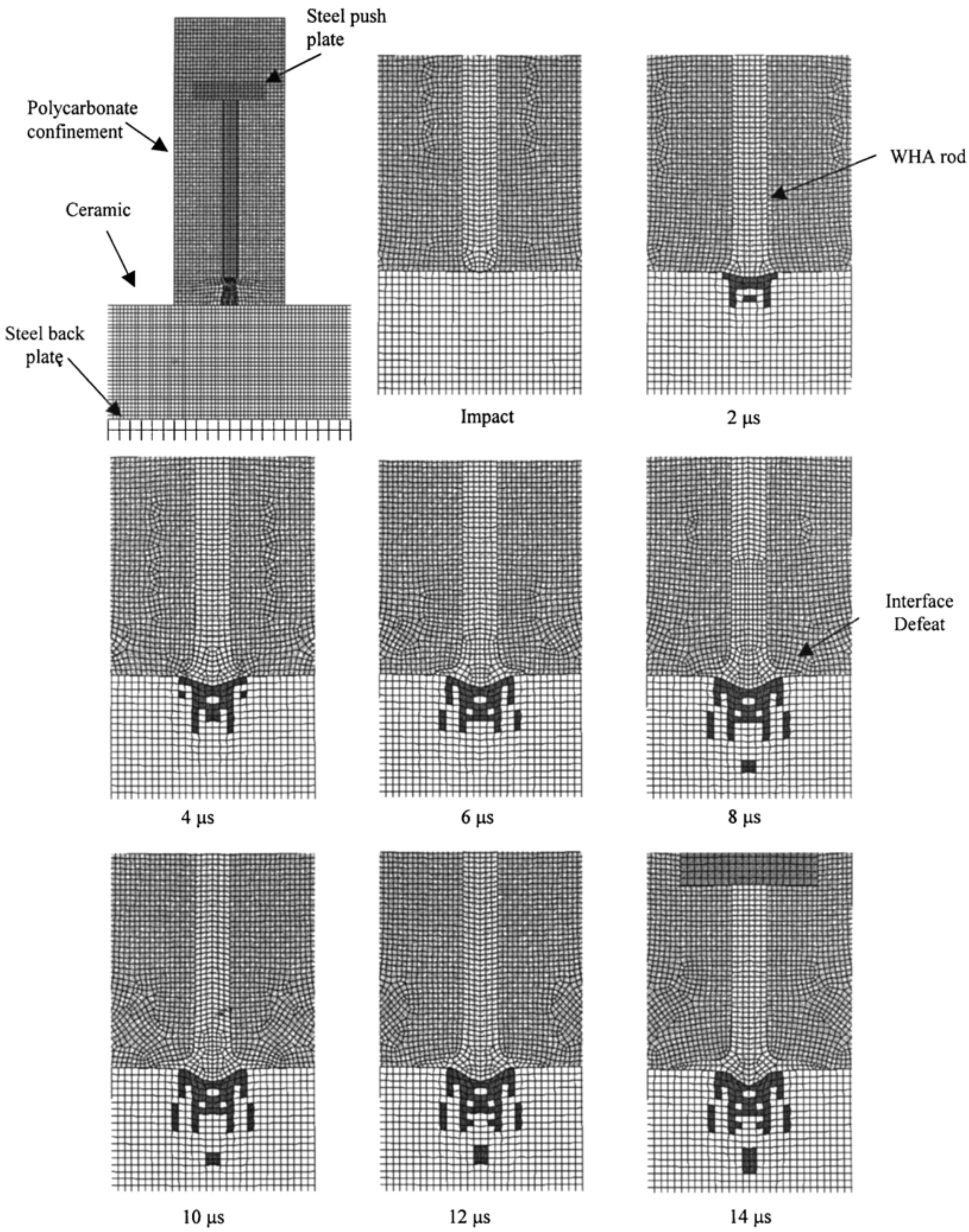

Figure 13. Simulation of the ID configuration. $V_{\text{impact}} = 1450\,\text{m/s}$. Elements in dark grey are integrated using the granular model.

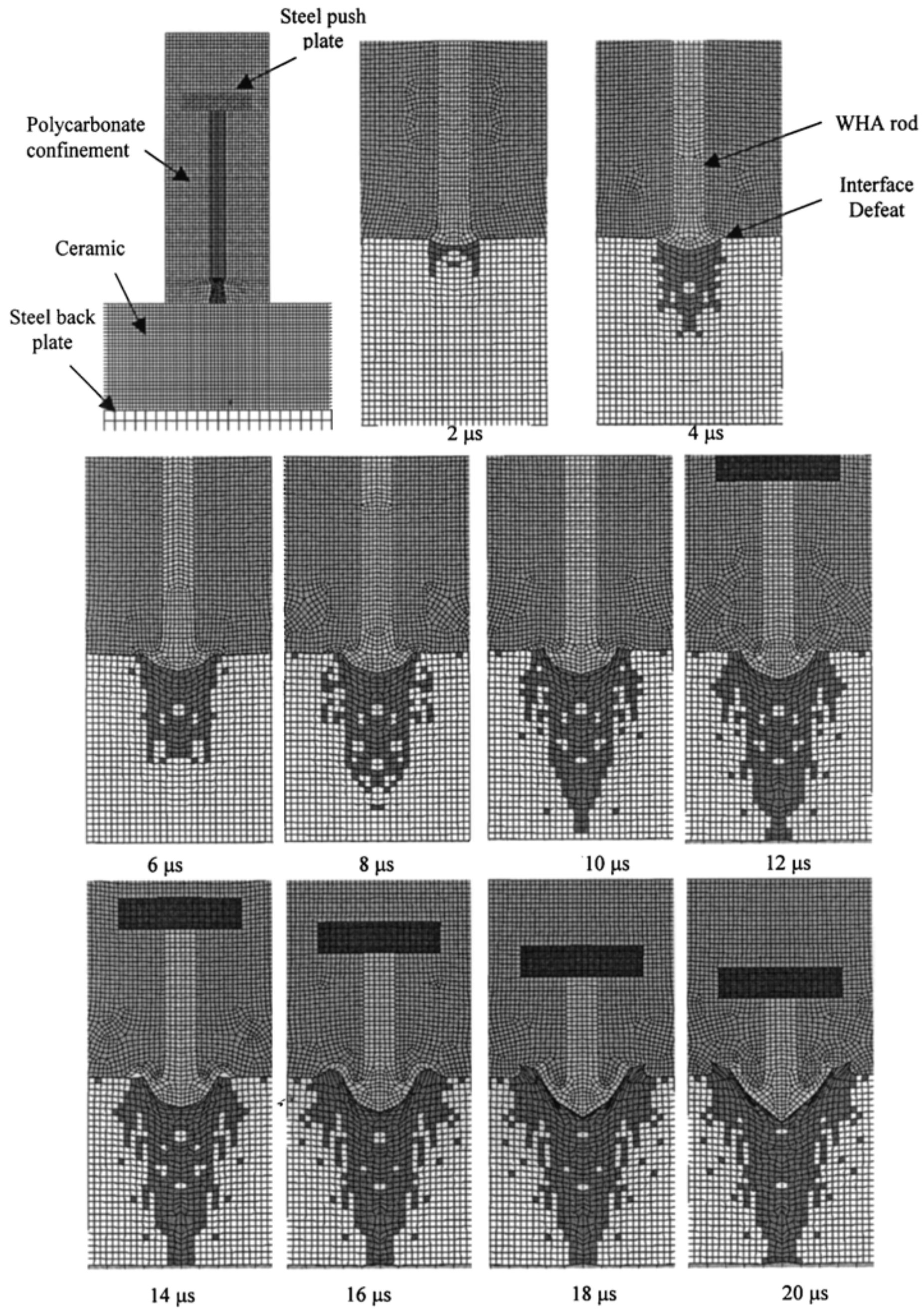

Figure 14. Simulation of the ID configuration. $V_{\text{impact}} = 1900\,\text{m/s}$. Elements in dark grey are integrated using the granular model.

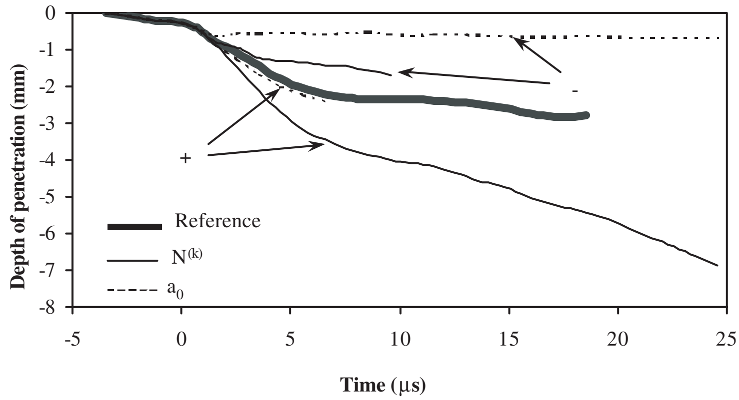

Figure 15. Depth of penetration versus time for different initial ceramic microstructures. + (respectively, −) indicates an increased (respectively, decreased) parameter relative to the reference case.

4. STUDY ON THE EFFECT OF MATERIAL PROPERTIES IN PENETRATION MECHANICS

A parametric study on the influence of the material properties has been carried out. The variation of each parameter is reported in Table V. We define as reference the value of the parameters previously identified and discussed. Meaningfully, variations are considered above and below the reference values.

4.1. Effects due to initial material microstructure

In the MPM model, microcracks density and initial length, on the various orientations, depend on ceramic initial microstructure. In the present case, the ceramic is considered isotropic in its initial state, i.e. microcrack length and density are supposed to be equal in all 13 planes describing the microstructure. The microcrack length and density used in the simulations are reported in Table V. As a measure of the model parameters effects, the depth of penetration versus time is plotted. In Figure 15, depth of penetration histories, when a_0 and N are increased or decreased with respect to a reference value, are shown. The time origin is the time at which the WHA rod impacts the ceramic front face.

There is no appreciable difference in the target behaviour during the early interaction of the polycarbonate sabot and the ceramic target. Similarly, in the first few microseconds of interaction between the rod and the ceramic, the penetration history shows no significant difference since at the point of contact the ceramic is instantly pulverized. After 2 μs the surrounding ceramic begins to play an important role as cracks propagate and the plate is fragmented.

The initial crack density directly affects the elastic cracking strain history. High initial density of defects results in ceramic fragmentation at early stages. As a result, displacement of fragments, at the penetrator tip occurs earlier. Furthermore, degradation of elastic moduli is accelerated, confinement of surrounding ceramic is decreased and projectile penetration is facilitated. Both these effects combine to control penetration rate. After a crater begins to form, the pressure at the interface remains higher than in the reference case.

Table V. Variation of parameters with respect to a reference set.

Effect	Parameter	Reference	Increased	Decreased
Initial microstructure	a_0	1 μm	2 μm	0.1 μm
	$N^{(k)}$	1000 mm^{-3}	10 000 mm^{-3}	100 mm^{-3}
Microcrack propagation	$n^{\pm}$	0.3	0.36	0.24
Critical cracking strain	ε_{cl}	0.15	0.18	0.12
Friction coefficient	P_{μ}	15 GPa	18 GPa	12 GPa
	μ_{cv}	0.05	0.06	0.04
	h_{μ}	300	360	240
	p	1.88		
Void ratio	E_2	5.0	6.0	4.0
	v_2	0.412236	0.4946832	0.329789
	η_{cr}	0.3	0.36	0.24
	η_m	0.3	0.36	0.24
	m	3.0	3.6	2.4
	n	2.84	3.408	2.272
	b	0.071	0.0852	0.0568
Dilatancy	h_{β}	2.0	1.6	2.4
Pressure cap	B	500.0	600.0	400.0
	M	1.2	1.44	0.96

On the contrary, a small defect density needs longer cracks before coalescence can occur. This takes more time and meanwhile the resistance of the ceramic is higher. During the first 5 μs, the projectile is defeated and consequently, the pressure at the interface decreases. Dynamic confinement is established and preserved during the entire interaction, see Figure 15.

Although the crack density is a constant in the model, it is worth noticing that the initial purity of a ceramic can play a very important role in the establishment of the interface defeat phenomenon. The longer it takes to generate cracks the higher the probability in attaining interface defeat.

Similarly, the size of the initial defects is directly related to the crack displacement jump and to the inelastic cracking strain histories. For large initial microcrack lengths, the fragmentation process occurs rapidly and the penetration rate increases. For small initial microcrack length the ID can be established before any significant penetration of the projectile, see Figure 15. It is noticeable that, for a given distribution of initial defects, a ceramic with small inclusions and small grain size should give a significantly better ballistic performance. The microstructure seems to have an important effect on the attainment of the ID mode.

4.2. Effects due to microcracks propagation speed

The parameters describing microcracks propagation are toughness (K_{Ic}) and coefficients $m^{\pm}$ and $n^{\pm}$, see Equation (4). The terminal crack velocity, controlled by parameter $m^{\pm}$, is approximately equal to $\frac{1}{3}$–$\frac{1}{2}$ the Rayleigh wave speed for a wide range of materials. Hence, $m^{\pm}$ is kept constant in this study. On the contrary, the power factor $n^{\pm}$, that represents the effect of crack propagation sensitivity to stresses, has been changed by 20 per cent.

Contrary to the initial material microstructure effect on penetration rate, the effect of crack velocity is negligible during the first 5 μs, even if a slight difference appears after 2 μs. Its role becomes noticeable after 5 μs but it does not result in a change in penetration rate, see

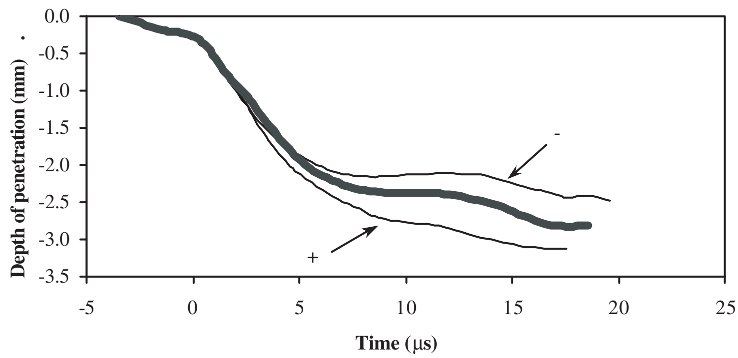

Figure 16. Depth of penetration versus time for different variations of the viscosity parameter $n^{\pm}$. $+$ (respectively, $-$) indicates an increased (respectively, decreased) parameter relative to the reference case.

Figure 16. The faster the microcracks propagate, the higher is the penetration rate. The lack of a noticeable difference in penetration history at early stages can be rationalized by the fact that it takes time for damage to accumulate to a sufficiently high level to result in some macroscopic manifestation.

4.3. Effects due to critical cracking strain

Pulverization is assumed whenever the critical cracking strain, ε_{cl}, or the maximum length of microcracks, a_{max}, is reached. In this study, the limiting cracking strain is set according to Table V. This variable describes the damage state of the ceramic at which microcrack coalescence leads to pulverization.

As long as cracks do not propagate, the ceramic response is elastic with a high yield stress. When cracks begin to propagate, the material stiffness drops achieving a very low level when the critical crack strain or a_{max} is reached. Then, longer cracks will not affect the material behaviour much. That is exactly what happens when the limiting cracking strain increases (see Figure 17). For low values of ε_{cl}, the stiffness of the damaged ceramic remains high and self-confinement occurs. This also implies that the ceramic granulates before microcracks propagate significantly, which is not realistic. For high values of ε_{cl}, the effective elastic response of the ceramic does not evolve any more and the depth of penetration is constant for increasing ε_{cl}. A realistic value of this parameter can be obtained by determining the value for which the depth of penetration begins to decrease. Furthermore, examination of stiffness variations in a representative volume element, modelled with the MPM model, is very helpful in identifying physically meaningful values of ε_{cl}.

4.4. Effects due to material internal friction

Internal friction resulting from friction between crack surfaces is an important physical parameter. In fact, crack sticking and therefore irreversibility may occur as a function of loading history. This parameter has a direct implication on ceramic damage under the point of impact. In the MPM model the variables are the factor p_{μ} and the values of μ_{min} and μ_{max}.

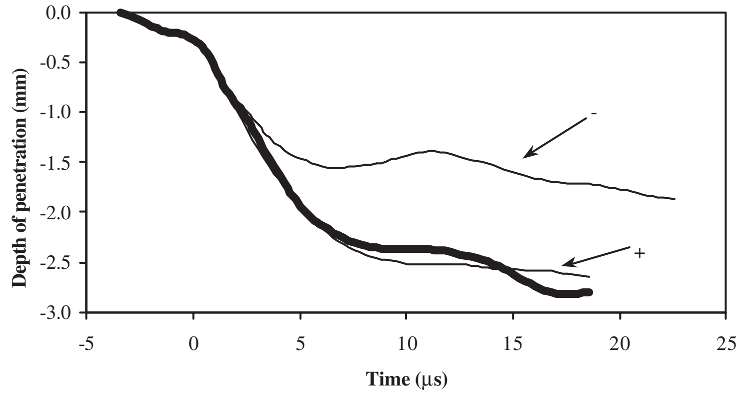

Figure 17. Depth of penetration versus time for different variations of the limiting cracking strain ε_{cl}. $+$ (respectively, $-$) indicates an increased (respectively, decreased) parameter relative to the reference case.

The minimum and maximum values of μ are the known values for ceramic materials. Only the dependence of the pressure factor is examined according to Table V.

When p_μ increases, μ becomes less dependant on the normal stress, sticking of crack surfaces occurs later in the process and the ceramic is subjected to more damage. This means that the ceramic offers not only less resistance to penetration but also that a larger volume of material is damaged. The self-confinement of the ceramic is then less efficient and fragments can be ejected. As a consequence, the depth of penetration increases as p_μ increases (see Figure 18). This can be sufficient to interfere with the beginning of the ID mode and the projectile may not be defeated. On the contrary, decreasing p_μ decreases the depth of penetration and the volume of damaged ceramic. This effect takes place only after 5 μs when ID occurs, see Figure 18.

An internal friction coefficient is also used in the granular model corresponding to the frictional effect between fragments. Its evolution depends on the current friction coefficient, the relative density and the plastic deformation due to the distortion mechanism. The material parameters are μ_{cv}, h_μ and p. It is difficult to extract the exact influence of these parameters as the equation of evolution for μ is coupled with the plastic deformation.

The parameters h_μ and p have an influence on the hardening coefficient h, which determines the rate of change of μ. When h_μ increases or when p decreases, the hardening coefficient increases. Therefore, it results in an increasing friction coefficient between fragments. Hence, self-confinement of the ceramic is certainly more efficient and the final penetration depth smaller. By contrast, an opposite change of the hardening modulus does not seem to affect the depth of penetration.

There is also a paradox in the influence of the parameter μ_{cv}. The depth of penetration increases when μ_{cv} increases. It should be noted that μ_{cv} is the minimum value of μ when the relative density decreases to η_{cr}. It is possible that this evolution is a modelling artefact. Note that these three coefficients neither interfere with the establishment nor the ID mode.

4.5. Effects due to fragmented material void ratio

The fragmented material void ratio has an influence on three well-defined aspects. First, it controls the elastic properties of the fragmented ceramic. Recall that Young's modulus

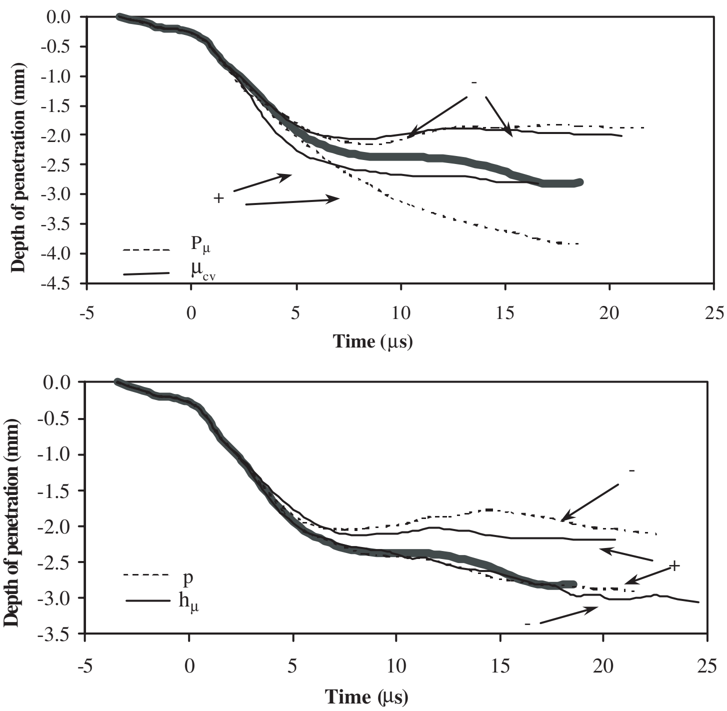

Figure 18. Depth of penetration versus time for different variations of the friction parameters. $+$ (respectively, $-$) indicates an increased (respectively, decreased) parameter relative to the reference case.

and Poisson's ratio are exponential functions of the relative density. Therefore, to assess the effect of void ratio, the functional coefficients have been changed according to Table V. The effects of variations in Poisson's ratio are not noticeable. At the same time, variations in Young's modulus do not affect significantly the results. As the void ratio remains very low during the deformation process, the variations in elastic properties also remain very small, see Figure 19.

Second, void ratio determines the relative density, which is limited by two characteristic values, η_m and η_{cr}. Once again, in the simulations, these values are never reached and their influence on the final penetration depth is negligible, see Figure 20.

Third, void ratio has a considerable influence on the evolution of some internal variables such as the pressure cap, p_c, the cohesion, c, and the friction coefficient, μ. As the cohesion of a dry ceramic is relatively low it is difficult to notice any influence of the parameter m. On the contrary, the parameter b that describes the influence of the void ratio on the friction coefficient is essential. A slight increase of b is enough to suppress the ID mode and to result in a steady penetration.

Increasing exponent n means increasing the influence of the void ratio on the pressure cap p_c. When n is higher, p_c decreases faster when the void ratio decreases. At the beginning of the projectile–ceramic interaction, the pressure under the impact point may not be high enough to reach the value of p_c and the projectile is arrested. After 10 µs, the pressure decreases

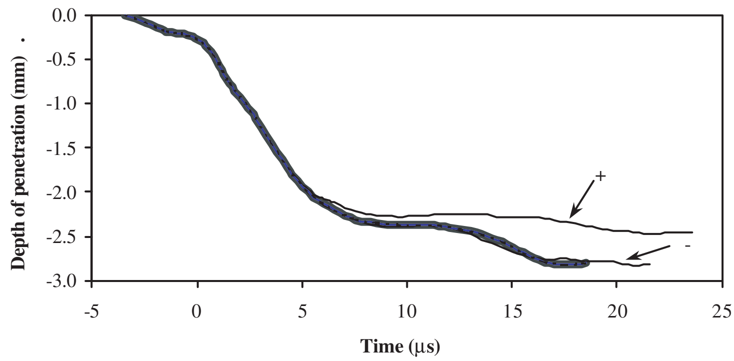

Figure 19. Depth of penetration versus time for different variations of the elastic properties as a function of relative density. Parameters E_2 and ν_2. + (respectively, −) indicates an increased (respectively, decreased) parameter relative to the reference case.

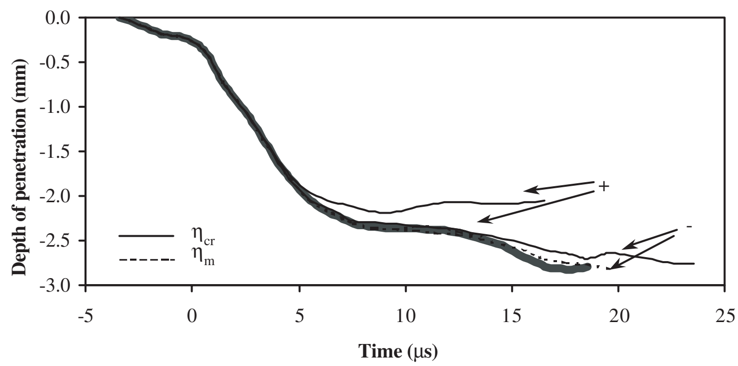

Figure 20. Depth of penetration versus time for different variations of relative density limits. Parameters η_{cr} and η_m + (respectively, −) indicate an increased (respectively, decreased) parameter relative to the reference case.

enough to allow the creation of voids in the ceramic. If the value of p_c decreases enough, then inelastic deformation can occur and the projectile begins to penetrate, see Figure 21. The ID mode is discontinued and a penetration mode is started. On the contrary, if p_c remains high, then the ID mode continues.

4.6. Effects due to material dilatancy

Dilatancy is controlled by the factor h_β and may be important in predicting shear localization in ceramic powders, see Espinosa and Gailly [29]. A variation of ±20 per cent in this parameter is examined, see Table V. As shown in Figure 22, the variation does not affect significantly the depth of penetration in the ID configuration. For a friction coefficient of about 0.2 and $\mu_{cv} = 0.05$, the change in h_β represents a change in dilatancy angle of about 20 per cent. It is interesting to note that when dilatancy increases, the projectile is defeated during a longer period of time. This first stage is followed by a small steady penetration mode as the pressure under the tip of the projectile increases, see Figure 22. The difference in penetration depth

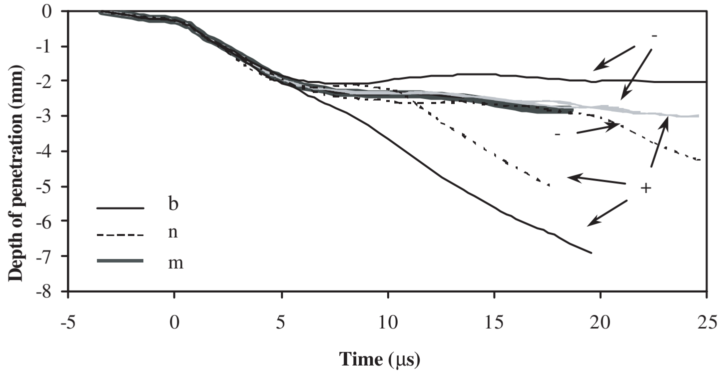

Figure 21. Depth of penetration versus time for different variations of b, n and m. $+$ (respectively, $-$) indicates an increased (respectively, decreased) parameter relative to the reference case.

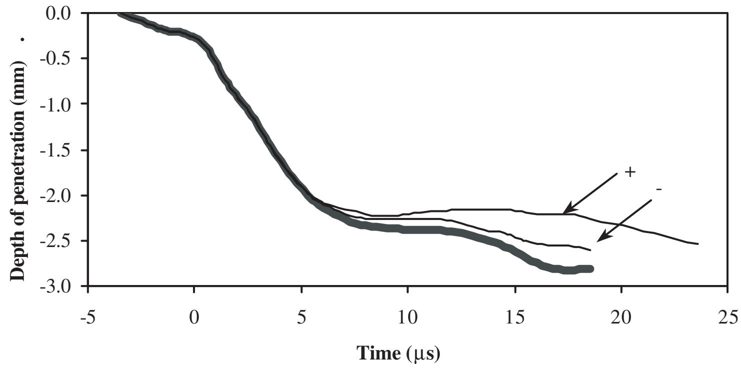

Figure 22. Depth of penetration versus time for different variations of the dilatancy parameter. $+$ (respectively, $-$) indicates an increased (respectively, decreased) parameter relative to the reference case.

and rate, between the reference case and the decreased dilatancy case, does not seem to be significant.

4.7. *Effects due to pressure cap*

The parameters affecting the yield surface for the consolidation mechanism are the shape factor M and the parameter B. B scales the critical pressure p_c. Both have been changed according to Table V.

The shape factor M does not affect the depth of penetration much. When M increases, the consolidation mechanism yield surface becomes more spherical. It also means that for a given pressure the yield stress increases. Consequently, the depth of penetration decreases slightly.

Variations in parameter B have no appreciable effect during the first 15 µs, see Figure 23. After this time, for the lower value of B, the projectile begins to penetrate at a high rate. The interpretation is the same as the one for parameter n. While the ID mode occurs, the pressure at the interface decreases. If this pressure drops below the pressure cap, then plastic deformation occurs and the projectile continues to penetrate. An increase in pressure occurs, at

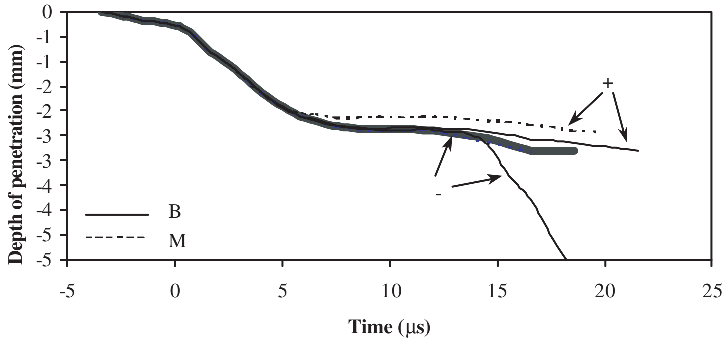

Figure 23. Depth of penetration versus time for different variations of the pressure cap parameters. + (respectively, −) indicates an increased (respectively, decreased) parameter relative to the reference case.

a later time, and its effect is to cause additional damage in the ceramic; hence, the penetration process cannot be stopped.

5. CONCLUDING REMARKS AND DISCUSSION

A new continuum model describing microcracking and flow of pulverized ceramic is presented. This deformation mode is observed experimentally in ballistic penetration of ceramic targets. The problem is extremely challenging from a computational standpoint, because it consists of the transition of material from its pristine state to a powder as a consequence of nucleation, propagation and coalescence of microcracks. Many models have been proposed in the literature to capture this physical phenomenon. However, none has successfully reproduced the observed failure modes as a function of ceramic confinement. Here, for the first time, penetration and ID of long rods striking multi-layered targets is captured computationally by a model whose parameters have been identified using other experimental configurations, namely, plate and rod impact experiments and cylinder collapse of ceramic powders.

In our model, damage in the ceramic is modelled by an elastic anisotropic formulation over 13 microcrack orientations. Flow of the pulverized media is modelled by two visco-plastic mechanisms with a non-associated flow rule. The transition between both models is realized when the inelastic cracking strain reaches a given critical value. The onset of pulverization, as determined by the response of a representative volume element modelled with the MPM model, provides key initial material properties needed in the granular model and a *consistent* transition between models.

The MPM/granular model has been implemented in the Lagrangian code LS-DYNA and used to reproduce the ID transition of an impacting tungsten long rod on a ceramic tile. Remeshing is used in the projectile to avoid the need of erosion. Penetration distances in depth of penetration and ID configurations proposed by Malaise *et al.* [8] are correctly reproduced. The extent of damage in the ceramic, under the point of impact, is in agreement with experimental observations. Furthermore, the velocity transition for change in penetration mode is also predicted.

Our simulations show that the prerequisite for penetration is the formation of a densely cracked zone in the ceramic ahead of the penetrator. The application of a high compressive stress in the front face of the ceramic limits the flow of damaged ceramic and leads to the onset of ID. The simulations also indicate that the formation of fragments is not sufficient to ensure continuous penetration since a compact granulated ceramic can self-confine. The ejection of previously formed fragments is also necessary for the projectile to penetrate. The pressure at the penetrator–ceramic interface seems to have a well-defined history as a function of projectile deformation mode. If the front face of the ceramic is confined, then the pressure remains high during the first few microseconds of interaction. This could be sufficient to keep the fragments closely packed. When the ID process starts the pressure drops to a lower level and the amount of damage in the ceramic does not grow significantly. On the contrary, if the front face of the ceramic is not confined or if the extent of the damage zone is large enough, then fragments are laterally displaced and ejected.

A parametric study was conducted to assess the effect of material microstructure, toughness, chemical purity, strength and stiffness on ballistic penetration mechanics. These sensitivity studies provide unique information on brittle materials response under various geometric configurations, i.e., degree of confinement. Our simulations show that the ID phenomenon is not very sensitive to the elastic properties of the ceramic. However, its microstructure, i.e. initial crack density, defects and grain sizes, are essential parameters. High purity ceramics with strong interfaces, low density of initial defects and small grain size appear to be the best candidates for armor design.

ACKNOWLEDGEMENTS

This research was supported by the Army Research Office through ARO-MURI Award No. DAAH04-96-1-0331 and by the Delegation Generale pour l'Armement through decision No.21132/DGA/DSP/D. The authors would like to convey these special thanks to Lallit Anand for providing the latest theoretical developments of his granular model.

REFERENCES

1. Mescall J, Weiss V. Materials behavior under high stress and ultrahigh loading rates—Part II. *Proceeding of the 29th Sagamore Army Conference*, Army Materials and Mechanics Research Center: Watertown, MA, U.S.A., 1984.
2. Shockey DA, Marchard AH, Skaggs SR *et al.* Failure phenomenology of confined ceramic targets and impacting rods. *International Journal of Impact Engineering* 1990; **9**(3):263–275.
3. Hauver G, Netherwood P, Benck R, Kecskes L. Ballistic performance of ceramic targets. *Proceedings of the Army Symposium on Solid Mechanics*, Plymouth, MA, U.S.A., 1993.
4. Hauver G, Netherwood P, Benck R, Kecskes L. Enhanced ballistic performance of ceramics. *Proceedings of the 19th Army Science Conference*, Orlando, FL, U.S.A., 1994.
5. Bless S, Ben-yami M, Apgar L, Eylon D. Impenetrable targets struck by high velocity tungsten long rods. *Proceeding of the 2nd Conference on Structures under Shock and Impact*, Portsmouth, U.K., 1992.
6. Rapacki E, Hauver G, Netherwood P, Benck R. Ceramic for armors—a material system perspective. *Proceeding of the 7th Annual TARDEC Ground Vehicle Survivability Symposium*, 1996.
7. Espinosa HD, Brar NS, Yuan G, Xu Y, Arrieta V. Enhanced ballistic performance of confined multi-layered ceramic targets against long rod penetrators through interface defeat. *International Journal of Structures* 2000; **37**(36):4893–4914.
8. Malaise F, Tranchet JY, Collombet F. An experimental investigation of ceramic block impenetrability to high velocity long rod impact. *Proceeding of the 6th International Conference on Mechanical and Physical Behaviour of Materials under Dynamic Loading*, Cracow, Poland, 2000.
9. Orphal DL, Franzen, RR, Piekutowski AJ *et al.* Penetration of confined aluminum nitride targets by tungsten long rods at 1.5–4.5 km/s. *International Journal of Impact Engineering* 1996; **18**(4):355–368.
10. Orphal DL, Franzen RR. Penetration of confined silicon carbide targets by tungsten long rods at impact velocities from 1.5 to 4.6 km/s. *International Journal of Impact Engineering* 1997; **19**(1):1–13.

11. Orphal DL, Franzen RR, Charters AC *et al*. Penetration of confined boron carbide targets by tungsten long rods at impact velocities from 1.5 to 5.0 km/s. *International Journal of Impact Engineering* 1997; **19**(1): 15–29.
12. Bruchey WJ, Horwath EJ. System considerations concerning the development of high-efficiency ceramic armors. *Proceeding of 17th International Symposium on Ballistics*. Midrand, South Africa, 1998.
13. Lundberg P, Renstrom R, Lundberg B. Impact of metallic projectiles on ceramic targets: transition between interface deformation and penetration. *International Journal of Impact Engineering* 2000; **24**:259–275.
14. Addesio FL, Johnson JN. A constitutive model for the dynamic reponse of brittle materials. LA-UR-89-2651, Los Alamos National Laboratory: Los Alamos, NM, U.S.A., 1989.
15. Rajendran AM, Grove DJ. Modelling the shock response of silicon carbide, boron carbide and titanium diboride. *International Journal of Impact Engineering* 1996; **18**(6):611–631.
16. Gurson AL. Porous rigid-plastic materials containing rigid inclusions-yield function, plastic potential and void nucleation. *Advances in the Research of Strength and Fracture of Materials*. vol. 2a. D.M.R. Tablin, Pergamon Press: NY, U.S.A., 1977.
17. Curran DR, Seaman L, Cooper T, Shockey DA. Micromechanical model for comminution and granular flow of brittle material under high strain rate application to penetration of ceramic targets. *International Journal of Impact Engineering* 1993; **13**:53–83.
18. Johnson GR, Holmquist TJ. An improved computational constitutive model for brittle materials. *High Pressure Science and Technologies*, vol. 2. AIP Press: Woodbury, NY, 1994; 981–984.
19. Collombet F, Malaise F, Tranchet JY. A numerical investigation of high velocity impact onto a ceramic block. *Proceeding of the 6th International Conference on Mechanical and Physical Behaviour of Materials under Dynamic Loading*, Cracow, Poland, 2000.
20. Klopp RW, Shockey DA, The strength behavior of granulated silicon carbide at high strain rates and confining pressure. *Journal of Applied Physics* 1991; **70**(12):7318–7326.
21. Sairam S, Clifton RJ. Pressure–shear impact investigation of dynamic fragmentation and flow of ceramics. *ASME AMD*, vol. 197, *Mechanical Testing of Ceramics and Ceramic Composites*, 1994.
22. Espinosa HD. On the dynamic shear resistance of ceramic composites and its dependence on applied multiaxial deformation. *International Journal of Solids and Structures* 1995; **32**:3105–3128.
23. Camacho GT, Ortiz M. Computational modeling of impact damage in brittle materials. *International Journal of Solids and Structures* 1996; **33**:2899–2938.
24. Ortiz M. Computational micromechanics. *Computational Mechanics* 1996; **18**(5):321–338.
25. Espinosa HD, Zavattieri PD, Dwivedi SK. A finite deformation continuum/discrete model for the description of fragmentation and damage in brittle materials. *Journal of the Mechanics and Physics of Solids* 1998; **46**(10):1909–1942.
26. Krysl P, Belytschko T. The element free galerkin method for dynamic propagation of arbitrary 3-D cracks. *International Journal of Numerical Methods in Engineering* 1999; **44**:767–800.
27. Belytschko T, Moes N, Usui S, Parimi C. Arbitrary discontinuities in finite elements. *International Journal of Numerical Methods in Engineering* 2001; **50**:993–1013.
28. Gu C, Kim M, Anand L. Constitutive equations for powder metals: application to powder forming processes. *Report of Research in Mechanics of Materials*. Department of Mechanical Engineering, MIT: Cambridge, MA 02139, U.S.A., 1999.
29. Espinosa HD, Gailly BA. Modeling of the shear instabilities observed in cylinder collapse experiments performed on ceramic powders. *Acta Materialia* 2001; **49**:4135–4147.
30. Dienes, John K. Statistical theory of fragmentation processes. *Mechanics of Materials* 1984; **4**(3–4):325–335.
31. Bazant ZP, Oh BH. Microplane model for progressive fracture of concrete and rock. *Journal of Engineering Mechanics*, *ASCE* 1985; **111**(4):559.
32. Espinosa HD. Micromechanics of the dynamic response of ceramics and ceramic composites. *Ph.D. Thesis*, Brown University: Providence, RI, 1992.
33. Espinosa HD, Raiser G, Clifton RJ, Ortiz M. Experimental observations and numerical modeling of inelasticity in dynamically loaded ceramics. *Journal of Hard Materials* 1992; **3**(3–4):285–313.
34. Freund LB. *Dynamic Fracture Mechanics*. Cambridge University Press: Cambridge, 1990.
35. Needleman A. Material rate dependence and mesh sensitivity in localization problems. *Computer Methods in Applied Mechanics and Engineering* 1998; **67**:69–85.
36. Simo JC, Kennedy JG, Govindjee S. Non-smooth multisurface plasticity and viscoplasticity. Loading/unloading conditions and numerical algorithms. *International Journal for Numerical Methods in Engineering* 1988; **26**:2161–2185.
37. Budianski B. Thermal and thermoelastic properties of isotropic composites. *Journal of Composites* 1970; **4**: 286–295.
38. Johnson GR, Cook WH. A constitutive model and data for metals subjected to large strains, high strain rates and high temperature. *Proceedings of the 7th International Symposium on Ballistics*, La Hague, 1983; 541–547.
39. Camacho GT, Ortiz M. Adaptive Lagrangian modeling of ballistic penetration of metallic targets. *Computational Methods and Applied Mechanics* 1997; **142**(3–4):260–301.

